SFG
371

School of Surveying

EARTHQUAKE COMMISSION

Strain accumulation across the central Southern Alps, New Zealand

—

A geodetic experiment to characterise the accumulation of strain

Paul Denys
Chris Pearson
Mikael Denham

Prepared for:

Earthquake Commission Research Foundation
Castrol House
36 Customhouse Quay
PO Box 311
Wellington
New Zealand

Tel: +64 (04) 499 0045
Fax: +64 (04) 499 0046

Prepared by:

School of Surveying
Otago University
PO Box 56
Dunedin
New Zealand

Tel: +64 (03) 479 7585
Fax: +64 (03) 479 7586

February 2005

Earthquake Commission Research Foundation Report 01/457

Contents

Abstract

The Alpine Fault is a major New Zealand geological feature. The fault boundary zone either side of the fault trace is deforming and it is this deformation in the central Southern Alps of New Zealand that we have measured and characterised in this project.

The region of interest includes a small network of permanently tracking or continuous GPS (CGPS and semi-CGPS) receivers located 30km south of Fox Glacier that extends between Karangarua (West Coast) and Mt Cook Village (East Coast). The network crosses both the Alpine fault and the main divide of the central Southern Alps. The Southern Alps Geodetic Experiment (SAGENZ) established the network of 12 sites in 2000 and it is the GPS data from the SAGENZ project that has been used to measure the horizontal deformation or more specifically, the strain across this tectonically active region.

In addition, GPS data observed during four epoch campaigns between 1994 and 2002 has been used. This data is part of the Institute of Geological and Nuclear Sciences (GNS) Global Plate Tectonics programme and covers a region of approximately 30 000km^2 of the Central South Island (CSI), roughly from the Rakaia River to the Waitaki River.

We have been able to measure horizontal velocities to better than ±1 millimetre per year (mm/yr). At this level of precision it is possible to investigate the velocity variation (i.e. velocity field) across the region and hence deduce the strain variation.

The data collected from the permanently tracking GPS sites has demonstrated that there are significant localised site displacements that appear to be induced by seasonal changes in the environment. The amplitude of the site displacements at several sites is as great as 5-8 mm, the largest is in the order of 20 mm. Although these displacements are not a direct function of the underlying tectonic forces, they do demonstrate the existence of localised strain variation and how dynamic the Southern Alps are.

The strain rates determined from the permanently tracking SAGENZ network were compared with the regional strain rates as determined from the CSI network. Generally the strain rates are in agreement, with the SAGENZ strain rate estimates being an order of magnitude more precise than the CSI rates. Although a direct comparison is difficult to make owing to the different sites used in each network, there are significant strain variations on a regional scale. In particular, from the smaller but greater density SAGENZ network, there is evidence of a zone of extension (which agrees with elastic dislocation theory).

Temporal strain variation was also investigated by determining the day to day strain variation relative to the long term site velocities, after removal of the seasonal site displacements. Although the signal is small, there appears to be times during the year when there is a greater degree of strain variability. For example, the spring to early summer period clearly has greater variability corresponding to an increase in daily temperatures and a corresponding increase in snow/ice melt. Conversely, the winter months tend to have less variability possibly due to snow and ice providing an insulating the underlying rock.

The average strain accumulation is consistent with the regional pattern, but there is evidence of regional variations that will not be observed using campaign measurements. Although the largest strain accumulation is derived from the collision at the plate boundary, there are more subtle strain variations being caused by seasonally induced processes.

Introduction

1.1 Project Objectives

This is a geodetic experiment, using an established Continuous GPS (CGPS) network crossing the Alpine Fault located in the central Southern Alps, to test the following two conjectures:

- That constant strain build-up is occurring over time, and;
- to compare this single transect with the (long term) average strain accumulation derived from campaign geodetic measurements that have been observed in the region.

The GPS data for this investigation have been collected by the Southern Alps Geodetic Experiment NZ (SAGENZ). To enhance the value of the data collected, it was proposed to use the GPS measurements to improve our understanding of the deformation process and hence earthquakes, in the central Southern Alps. Firstly we aim to compare our localised strain rates with those determined largely by averaging the rates determined from GPS campaigns since 1994. Secondly, we can determine, from the time series data, if the strain accumulation is uniform in nature, or if this rate is changing. Since the project is to continue over a five year period, it seemed reasonable that it may be possible to determine if there are other periodic fluctuations (e.g. seasonal, yearly variations) that may be driven by other factors such as climatic conditions.

1.2 Project Merit

Our current knowledge of the recurrence of an earthquake on the Alpine Fault is based on palaeoseismic evidence (including forest age and tree ring chronologies) derived using data spanning time scales from 100's to 1000's of years. To verify the applicability of this long-term evidence to current processes, we are endeavouring to understand the present-day deformation rates of the Alpine fault zone and the processes responsible for them using near-real time continuous measurements rather than through discrete geodetic campaigns (nominally at intervals of 2-3+ years). Recent geodetic work provides a reliable measure of the strain rates over most of the South Island, but will average the deformation signal at a regional scale. Variations in both the spatial uniformity and temporal persistence of the signal may exist and although currently the cost of installing a (large) dense network of GPS receivers in the Southern Alps to determine any variations would be prohibitively expensive, we can study this central Southern Alps transect in a region that has a relatively low level of recorded seismicity. It is a small but significant project that can demonstrate the geodetic component of a hazard monitoring program.

Although the region is relatively remote, it is likely to produce a major earthquake with a rupture length longer than most other earthquakes that would significantly affect central South Island locations. Knowledge of the strain rate and possible variations is significant if we want to improve our understanding of earthquake recurrence in this region. The central Southern Alps region is important in evaluating the seismic hazard of the central South Island.

1.3 Project Background

This research project uses GPS data collected by the SAGENZ project. For completeness, a brief outline of the SAGENZ programme is given.

The data for this investigation are currently being collected through a collaborative project between Otago University (OU), the Institute of Geological and Nuclear Sciences (GNS), the Massachusetts Institute of Technology (USA) and the University of Colorado at Boulder (USA). The purpose of the SAGENZ project is to measure the rates and distribution of vertical uplift across the Southern Alps. The project was initiated in 1999 when a potential transect and sites were identified. Monuments were subsequently constructed and equipment installed in early 2000.

Since 2000, we have deployed a total of 10 GPS receivers. These receivers have been established on a profile that crosses the central Southern Alps. The profile extents from the west side of the Alpine Fault, in the vicinity of the Karangarua settlement, across the main divide to the Mount Cook village with a further site at the Mt John Observatory (Lake Tekapo). Between the Alpine Fault and the main divide, the receivers have been placed in a corridor on predominately east-west orientated ridge lines. The profile is located along ridgelines for good sky visibility. The data from the continuous sites are downloaded at least once per day using a radio telemetry system. This data are then transferred to data archives via the internet and are routinely processed to generate a time series for all three position components (East, North and Up).

This EQC Foundation Research project has utilised the SAGENZ data set to determine if the strain rate is uniform through time and to compare the strain determination with the campaign GPS strain estimates.

1.4 Report Outline

The report includes two background sections. Section 2 gives a brief overview of tectonics in New Zealand, in particular South Island tectonics and the geodetic contributions. Section 3 outlines the major data processing options and broad methodology used, including software used, to estimate the geodetic parameters, network combination and analysis and the strain rate parameter estimation.

A description of the GPS networks and GPS data is given in Section 4. An overview of the SAGENZ network is given, including the monumentation, equipment and operation of the semi-CGPS and CGPS sites. The network parameter estimates, data characteristics and trends of the processed data is given. This includes the network velocity field, position offsets (due to antenna changes) and some examples of site time series for the horizontal coordinate components. Overall data quality is characterised using the positional rms values determined from daily coordinate repeatability.

The results are given in two sections that consider the long term strain rate (Section 5) and temporal strain (Section 5.3) of the SAGENZ network. The long term strain rate is determined from both the Central South Island (CSI) and SAGENZ networks and includes estimates of the engineering and eigenvalues strain estimates and areal dilatation. Comparisons are also made with the strain rates determined from 4 years of data in Beavan *et al.* (1999). The final section investigates possible temporal strain based on SAGENZ sites with long periods of continuous data.

2 Review of New Zealand Tectonics and Geodesy

Geodetic studies of South Island tectonics started with the innovative work of Bibby (1975; 1976) who demonstrated that conventional survey data could be analyzed using shear strain rates. Earlier attempts were plagued with problems due to the relatively poor determination of distances compared to angles measurements. Building on this work, Walcott (1978; 1979) made a comprehensive study of repeated survey measurements undertaken in the South Island that had been serendipitously made by New Zealand Government Surveyors during their normal duties in support of traditional land survey applications. The success of these early studies caused a series of survey networks to be established specifically for the purpose of measuring tectonic strain accumulation in the South Island. There were two types of networks: (1) a series of small scale fault monitoring patterns with dimensions of a few kilometres that were established across major faults (Wood and Blick 1986) and (2) at a larger scale, a series of three major earth deformation networks with inter-station distances of 10-20 km that were established to span the island and thus cross the entire plate boundary zone (Hannah 1984). The results of all of the studies of conventionally derived geodetic data were synthesized by two major regional studies by Bibby *et al.* (1986) and Reilly (1986).

After a pause of several years, geodetic investigations in New Zealand resumed with a GPS transect between Christchurch and Hokitika in December 1992 (Pearson *et al.* 1995). This work continued in a series of annual campaigns whose results are discussed below. Much of this work was synthesized by Beavan and Haines (2001).

2.1 *Summary of Tectonics of the South Island*

The tectonics of the far south of the South Island is dominated by the Puysegur subduction zone and the Alpine fault that continues off shore along most of the Fiordland coast. The existence of subduction in Fiordland was originally identified by Davey and Smith (1983) on the basis of the distribution of earthquake hypocenters. Their early understanding of the structure of the Puysegur subduction has been recently refined and updated by Eberhart-Phillips and Reyners (2001). The basic model still shows a well defined seismically active zone extending along the length of Fiordland that dips very steeply in the north and more gently in the south.

There has been very little geodetic investigation in the Fiordland region. Walcott (1978) and Pearson (1992) both studied shear strain in the Waiau Basin, however, since there were no geodetic quality conventional surveys in Fiordland any studies in Fiordland proper had to wait till the advent of GPS. Since then, one study has been conducted by Pearson (1998), which he interpreted as supporting full locking on the Puysegur Plate Boundary Thrust.

In the central part of the South Island, located roughly between Haast Pass and Arthurs Pass, two largely submerged continental fragments, the Challenger Plateau and the Chatham Rise, collide obliquely. In the collision zone, the plate boundary is marked by the Alpine fault, which is a relatively straight through-going fault. Within this region the Alpine fault is an oblique slip fault that accommodates both the strike-slip and convergent components of plate motion (Norris *et al.* 1990). Norris *et al.* shows that, while close to the surface it is divided into a series of strike and dip-slip segments at depth, the Alpine fault is a single planar fault whose slip vector is parallel to the relative plate motion vector. Geodetic studies (Beavan *et al.* 1999; Pearson *et al.* 2000) and geological analysis (Norris and Cooper 1995) show that the Alpine fault accommodates about 75% of the relative plate motion. The character of the

Alpine fault is not uniform along strike, however. South of the Cascade River the Alpine fault is a steeply dipping strike-slip fault with very little dip-slip motion (Hull and Berryman 1986; Sutherland and Norris 1995), whereas further north the Alpine Fault is a 55° dipping oblique slip fault accommodating both reverse and strike-slip motion. Recent palaeoseismic studies, summarized by Norris and Cooper (2001), imply slip rates of 24 - 27 mm/yr strike-slip and 10 - 0 mm/yr dip-slip with the highest dip-slip rates in the central segment of the Alpine fault and decreasing toward zero south of Haast Pass. Both surface geological measurements (Sibson *et al.* 1979) and geophysical studies (Davey 1998) show that at depth, the Alpine fault can be traced as a 55° east dipping plane well into the ductile regions of the crust. Leitner *et al.* (2001) shows that the locking depth on the Alpine fault and Marlborough faults is about 12 km, which is similar to values determined from the inversion of geodetic data by Beavan *et al.* (1999) and Pearson *et al.* (2000). The Alpine fault passes offshore at Milford Sound, however, the fault is known to continue offshore on a trend generally paralleling the West Coast of Fiordland until it merges with the Puysegur Trench off southern Fiordland (Lebrun *et al.* 2003).

The first geodetic investigation of the Alpine fault by Walcott (1978) studied the area around Okarito in central Westland. This was followed by Pearson's (1991) study of the repeated triangulation data from a corridor extending from the West Coast across Haast Pass. The first study of the Alpine fault using GPS geodesy was done by Pearson *et al.* (1995) who repeated the Christchurch to Hokitika earth deformation network. This was followed by Beavan *et al.* (1999) with a network that crosses the central segment of the Alpine fault in the area of highest uplift. Pearson *et al.* (2000) investigated the Alpine fault at Haast Pass in the transition region between the oblique slip and strike-slip segments of the fault. Both of the later two studies used only GPS data for both epochs.

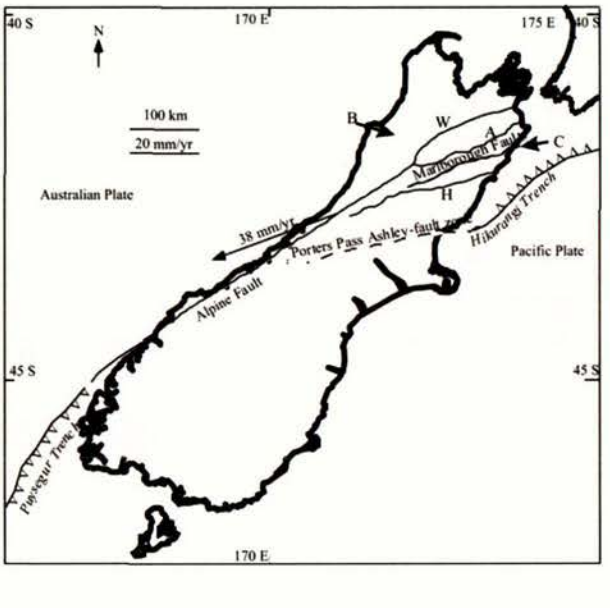

Figure 1: Simplified Tectonic Map of New Zealand. H is the Hope Fault, C is the Clarence Fault, A is the Awatere Fault, W is the Wairau Fault and B shows the location of the Buller region

In the northern end of South Island, the Alpine fault becomes part of a broad zone accommodating the collisional tectonic regime in the central South Island and the subduction associated with the Hikurangi Trench. Within this zone the major structures are the Marlborough faults, a series of northeast-southwest trending strike-slip faults (the Wairau, which is a continuation of the Alpine fault, Awatere, Clarence and Hope faults) that accommodate most of the relative plate motion (e.g. Cowan 1990; van Dissen and Yeats 1991; Berryman *et al.* 1992; Cowan 1992; Holt and Haines 1995; McCalpin 1996; Yetton *et al.* 1998). The Hope fault, the southernmost of the recognized Marlborough faults, is also the most active with slip rates of 20 - 25 mm/yr, and is more than twice the rate for any of the northern faults (Van Dissen and Yeats, 1991). The Wairau and Awatere Faults have estimated slip rates of 4-6 mm/yr and 5-10 mm/yr respectively (Holt and Haines 1995). Northwest of the Wairau fault, shortening occurs in the Buller region (see Figure 1). This region is the locus of two of the largest earthquakes (Murchison 1924 and

Inangahua 1968) that have occur in the South Island during the last hundred years. There is also some evidence that the Porters Pass fault, whose surface trace extends for only about 40 km north-east of Lake Coleridge, is part of a through going dextral strike-slip feature, the Porters Pass-Amberley fault zone (PPAFZ), some 60 km south of the other Marlborough faults (Cowan 1992; Anderson *et al.* 1993; Holt and Haines 1995; Cowan *et al.* 1996). If so, this fault zone may be part of a southward progression of the Marlborough fault system.

Surprisingly, since the Marlborough Faults were the subject of some of the earliest geodetic studies in New Zealand (e.g., Bibby 1975), there has only been one GPS based study of the region. This study by Bourne *et al.* (1998) appeared to support the geodetically determined slip rates for the Marlborough Faults.

In the southeastern reaches of the North Island, the Hikurangi Trench accommodates much of the convergent component of relative plate motion with virtually all of the strike-slip motion accommodated by two major strike-slip faults (e.g. the Wairarapa and Wellington Faults, Beanland (1995). Using seismological data, Reyners *et al.* (1997) concluded that the subduction interface in the northern South Island has become locked within the last 4 Ma with the deformation now occurring on the Marlborough Faults in continental crust of the South Island (Walcott 1998).

3 Methodology

Geodetic measurements of (discrete) station positions derived from GPS observed data provide important constraints on the kinematics of the Earth's crust. Over time, from either epoch style campaigns or Continuous GPS (CGPS) networks, it is possible to determine highly precise station velocities. Combining several stations together to form a network enables a regional velocity field to be determined. A change in the velocity field, i.e. velocity gradient, implies a regional deformation field. Conversely if the velocity field is uniform, then the region is translating without deformation. Strain or strain rates can be calculated from the gradient of the velocity.

Our aim is to compute deformation parameters from observed GPS data collected from our small regional network. We process and analysis the GPS data in a three step process:

1. **Geodetic Parameters:** The GPS data is processed on a daily basis to provide loosely constrained estimates of the station coordinates (geodetic parameters).
2. **Network Combination and Analysis:** The daily solutions (loosely constrained) are combined to form a single network solution (station coordinates and velocities). Position and velocities minimal constraints are imposed to define a uniform reference frame.
3. **Deformation Parameters:** Different combinations of strain or strain rate parameters are computed based on the station coordinates and velocities.

In addition to the primary parameters (geodetic and deformation parameters), the process allows for the estimation of auxiliary parameters that account for time-dependent displacements (e.g. seasonal effects) or changes in instrumentation (e.g. antenna changes).

The GPS data processing has been undertaken using the Bernese GPS software (Step 1) and the combination of the daily network solutions plus estimation of auxiliary quantities has been undertaken using Quasi-Observation Combination Adjustment (QOCA) software (Step 2). QOCA is also used to determine the deformation parameters (Step 3). More detailed steps and processing options are described in the following section.

3.1 Geodetic Parameter Estimation

The GPS data were processed with the Bernese Post Processing Software Version 4.2 (Hugentobler *et al.* 2001) using the Bernese Processing Engine (BPE). The BPE enables the automation of data processing and is especially designed to process, in a coincident manner, a network of sites and hence estimate station coordinates (geodetic parameters). As the data processing procedures are well established and documented, only a brief outline will be given.

Using the Bernese software, a daily set of station coordinates is estimated based on the processing of all simultaneously observed data over one day (24 hours) using the carrier phase double difference observable forming the ionosphere-free linear combination. During the processing, decisions must be made with regard to satellite orbits and Earth Orientation parameters used, the method of removing the troposphere bias, and the measurement model corrections for tidal effects.

For each day a final set of geodetic parameters (station coordinates and variance-covariance matrix) is estimated. This solution is generated as a loosely constrained set of coordinates based on a subset of International GPS Service (IGS) stations in and close to New Zealand. These coordinates are in terms of the International Terrestrial Reference Frame 2000 (ITRF2000) station coordinates and velocities with loose constraints of 0.1m (10cm). The Bernese daily solution is saved in the SINEX[1] format and subsequently used as input to the QOCA processing.

Basic observables	GPS carrier phase: L1, L2. (Code measurements are used for receiver clock synchronization) Elevation cut-off angle 5°plus elevation dependent weighting Data sampling rate 30 seconds used during pre-processing and 600 seconds for final solution
Modelled observable	Double-difference carrier phase, ionosphere-free linear combination.
Ground antenna phase centre calibrations	Elevation-dependent phase centre corrections are applied according to the model IGS_01. The corrections are given relative to the AOAD/M_T antenna.
Troposphere	No a priori troposphere model used The Niell mapping function is used.
Ionosphere	Not modelled but eliminated by forming the ionosphere-free linear combination of L1 and L2. A regional ionosphere map is generated in order to improve the QIF ambiguity resolution.
Orbits and ERPs	IGS final orbit and ERP information adopted DE200 planetary ephemerides JGM3 geopotential model Ocean loading applied
Tidal displacements	Solid earth tidal displacements are modelled according to IERS conventions 1996. Ocean loading corrections are computed based on Scherneck's amplitudes and phases No atmospheric loading corrections are taken into account

Table 1: Bernese processing measurement models

A brief description of the processing options used for the various measurement models and estimated parameters are given in Table 1 and Table 2 respectively.

[1] Solution Independent Exchange Format

Troposphere	Zenith path delay parameters are solved for at 2-hour intervals for each station.
Ambiguities	Ambiguity resolution is performed by using the quasi-ionosphere-free (QIF)
Satellite clock biases	Satellite clock corrections are not estimated but eliminated by forming double differences
Receiver clock biases	Receiver clock corrections are estimated as part of the pre-processing using code measurements. They are finally eliminated by forming double differences.
Coordinates and variance-covariances	Final three dimensional coordinates and full variance-covariance matrix are output in both the Bernese and SINEX formats.

Table 2: Bernese processing estimated geodetic parameters

3.2 Network Combination and Analysis

To combine geodetic measurements and derived parameters from various techniques quantitatively, the Earth's shape and change in shape over time needs to be parameterised using common parameters. Such choices include, for example baseline length, baseline azimuth, network strain (or strain rate). In the era of the modern space geodesy, the most commonly used parameters are the 3-dimensional time-dependent station positions. The Quasi-Observation Combination Analysis (QOCA) software package combines various loosely constrained coordinate and velocity solutions (as quasi observations) to obtain crustal deformation information. A detailed description of the QOCA methodology and algorithms is given in (Dong *et al.* 1998).

With the development of CGPS, even small networks generate large quantities of data that need to be combined in an efficient manner. Typically the analysis of geodetic data is carried out by combining (or aggregating) normal equations or using station coordinate and variance-covariance matrices. QOCA solves for site positions, velocities, coordinate system parameters, and will also parameterise coseismic/postseismic deformation and seasonal displacements simultaneously. Crustal deformation parameters such as strain or strain rates can also be obtained. The QOCA software has been used in various geodynamics studies ranging from the determination of regional strain rates (e.g. Feigl *et al.* 1993; Bock *et al.* 1997; Hager *et al.* 1999; Shen *et al.* 2000; Shen *et al.* 2001) to seasonal displacements (e.g. Soudarin *et al.* 1999; Mangiarotti *et al.* 2001; van Dam *et al.* 2001; Dong *et al.* 2002; Zhang *et al.* 2002)

The classical solution involves the global inversion of all observed data at all stations to estimate station coordinates and velocities as well as auxiliary parameters for periodic seasonal terms and position offsets. Such an inversion has the advantage of using the full variance-covariance matrix and therefore accounts for parameter correlations. However, it does have the disadvantage that any outlier observation(s) or unmodelled biases have the potential to affect several parameters. With longer time series and an increasing number of sites, this approach can also be a computational burden.

The GPS site coordinates and their variance-covariance matrices (SINEX format) are used as input to QOCA as quasi-observations. This combination is performed by sequential Kalman filtering that combines all the daily solutions and models the plate tectonic motion with a constant velocity. A consistent reference frame is achieved by constraining several IGS sites and allowing for a daily network translation and rotation. The constrained IGS stations, Whagaparaoa (AUCK), Chatham Island (CHAT), Hobart (HOB2), Townsville (TOW2) and Macquarie Island (MAC1), are sufficiently far from the region of interest (the central Southern Alps) not to be affected by localised network noise.

The combination process must also deal with appropriate weighting of the quasi-observations (covariance scaling), outlier detection, seasonal displacements and position offsets. The rescaling of the variance-covariance matrix is achieved through error analysis procedures outlined in (Dong *et al.* 1998). Error modelling can be problematic since least squares algorithms assume a white noise process and, as the error spectra of GPS positions include spatial correlations (common orbits, earth rotation, regional atmospheric bases, (e.g. Feigl *et al.* 1993)), and temporal correlations (atmospheric disturbances, monument instability (e.g. Zhang *et al.* 1997; Mao *et al.* 1999)), individual site errors are not easily isolated. After removing outlier observations, usually caused by unmodelled systematic errors, it is necessary to scale the variance-covariance matrix as most GPS processing tends to under-estimate the effective data noise contained in variance-covariances.

To rescale the variance-covariance matrix, a non-rigorous but realistic estimate of the data uncertainties is used based on the (uncorrelated) data sampling rate (see e.g. Feigl *et al.* 1993; Zhang *et al.* 1997). The Kalman filter is run iteratively (forward and back) through the input data. When new data is added to the Kalman filter while propagating to a new epoch, the incremental weighted sum of squared residuals $(\delta\chi^2)$ provides an estimate of the consistency of the new data with the total solution. The square root of the $\delta\chi^2$ for each daily solution, averaged from the forward and backward Kalman filtering, is used to rescale the associated daily variance-covariance matrix (Dong *et al.* 1998).

Once the outlier observations have been removed and appropriate covariance matrix scaling applied, the position offsets (typically caused by antenna changes) and periodic seasonal terms are estimated together with station coordinates and velocities in a consistent reference frame. We estimate the magnitude and phase of semi-annual and annual terms (total of up to 6 parameters per site) and, where appropriate, offsets in the time series (e.g. antenna changes). The periodic terms contained in the station time series are fitted using the sine function with

$$\Delta_{periodic} = A\sin[\omega(t - t_0) + \phi_0]$$

where the two estimated parameters are A = amplitude and ϕ_0 = initial phase. For the annual term $\omega = 2\pi/year$; for the semi-annual term $\omega = 4\pi/year$; t_0 = initial epoch (e.g. 2000.0) and t = time in years.

Although deformation parameters, e.g. strain or strain rates can also be estimated in QOCA simultaneously, it is typical in deformation analysis to test different network partitions and station combinations over several reruns. A more computationally efficient approach is to use QOCA to generate the velocity field and full velocity variance-covariance matrix. A separate QOCA strain analysis utility can then be used to compute strain rates based on different station combinations.

3.3 Strain rate estimates

As the Earth's crust is subjected to stress, the fractional change in shape (volume) is called strain (ε). This is normally expressed in a change of volume per unit volume. A solid (e.g.

the Earth's crust) will respond to stress elastically until a critical stress is reached. Beyond the elastic limit, brittle material will deform by fracturing and ductile material will deform by flowing. The elastic limit is a function of pressure and temperature.

Geodetic (and seismic) methods are used in plate boundary zones to detect and measure deformation. To do this, the estimation of strain rates from geodetic data can be based on three equivalent parameterisations (Feigl *et al.* 1990). These include describing the velocity field in terms of the velocity gradient, while the eigenvalue or engineering shear parameters are the two most common parameterisation methods that are more easily compared with geophysical observations. Both are defined here.

3.3.1 Eigenvalue Parameterisation: $\dot{\varepsilon}_1, \dot{\varepsilon}_2, \theta, \dot{\omega}$

The eigenvalue parameterisation of a two-dimensional velocity field includes strain rate eigenvalues: maximum extension strain rate, $\dot{\varepsilon}_1$, and maximum contractional strain rate, $\dot{\varepsilon}_2$, in the directions of the principal axes of extension $(\hat{\mathbf{e}}_1)$ and compression $(\hat{\mathbf{e}}_2)$. By convention, extension is positive with $\dot{\varepsilon}_1 > \dot{\varepsilon}_2$.

The angle θ is the direction of the principal axes of compression $(\hat{\mathbf{e}}_2)$ from the north axis, measured clockwise. An arbitrary rigid body rotation rate is defined by $\dot{\omega}$ to account for a non-symmetric velocity gradient, but is generally not well defined from geodetic observations and therefore not often determined.

3.3.2 Engineering Shear Parameterisation: $\dot{\gamma}_1, \dot{\gamma}_2, \dot{\bar{\varepsilon}}, \dot{\omega}$

The engineering parameters $\dot{\gamma}_1$ and $\dot{\gamma}_2$ are used to describe the angular shear strain rate components. These values can be given a geophysical interpretation in terms of either simple shear or pure shear (see Feigl *et al.* 1990). The rate of areal dilation is defined as the sum of the two strain rate components $\left(\dot{\bar{\varepsilon}} = \dot{\varepsilon}_1 + \dot{\varepsilon}_2\right)$ and represents the net increase (positive) or decrease (negative) in the area over which the strain rate is computed. The rotation, $\dot{\omega}$, is the same as defined in Section 3.3.1.

Two derived quantities include the maximum engineering shear rate, $\dot{\Gamma}$, and principal direction of contraction, β, with

$$\dot{\Gamma} = \sqrt{\dot{\gamma}_1^2 + \dot{\gamma}_2^2}$$

$$\beta = \tan^{-1} \frac{-\dot{\gamma}_2}{\dot{\gamma}_1}$$

The principal direction of contraction (β) is related to the direction of the maximum right lateral shear (θ) by the expression

$$\beta = \theta + 45^\circ$$

4 Network and Data Characteristics

4.1 The Central South Island (CSI) Network

The CSI network has been observed using epoch styled GPS campaigns in 1994, 1996, 1998 and 2002. Beavan *et al.* (1999) comprehensively described the network and data analysis for the first three campaigns, and so this information will not be repeated here. The fourth campaign in 2002 largely repeated the same network sites. This report uses the results of the combined four campaigns, making some limited comparisons with the results in Beavan *et al.* (1999). The extent of the network (shown in Figure 2) stretches from the East to West Coasts of the South Island, and between the Rakaia and Waitaki Rivers. .

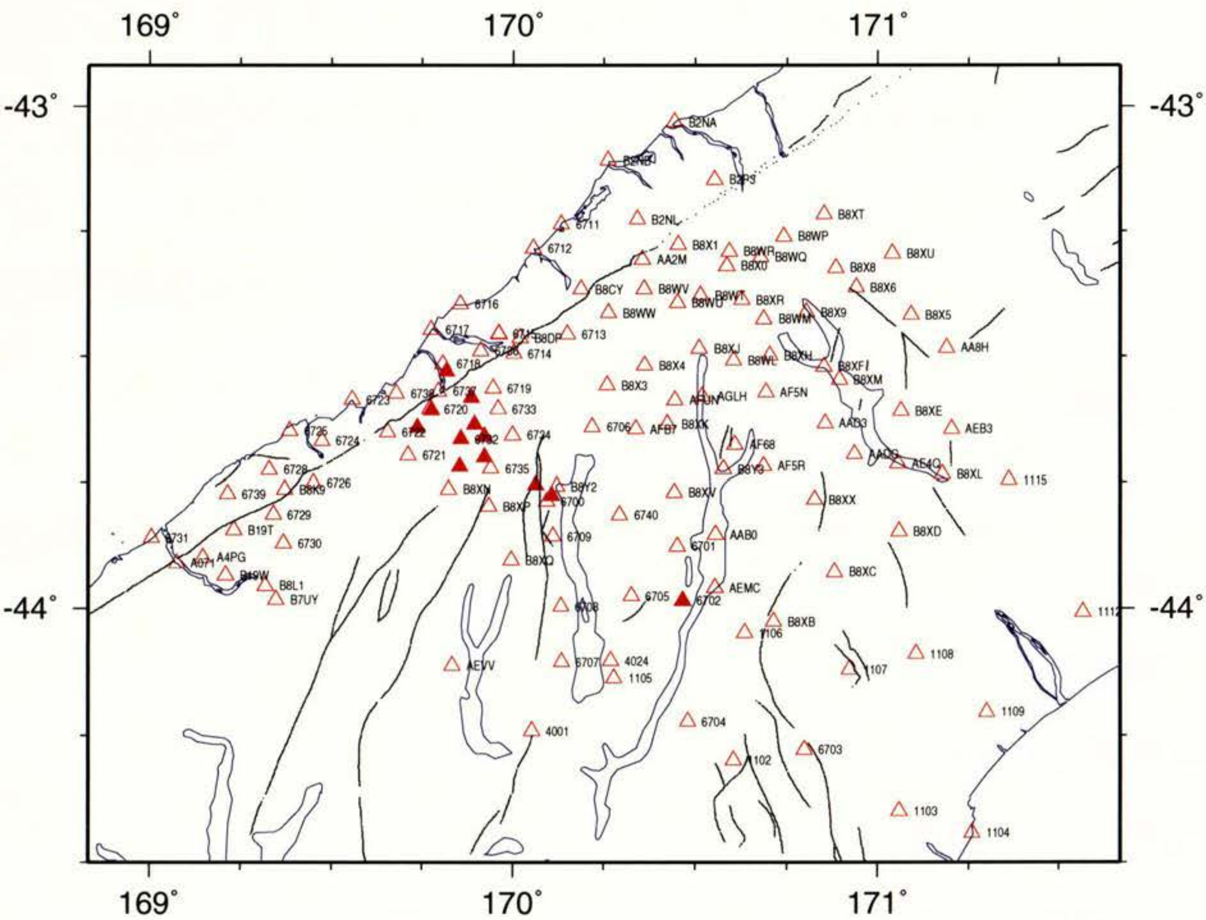

Figure 2: The Central South Island (CSI) network sites shown as red triangles (no fill). Solid red triangles indicate locations of the SAEGENZ sites (see also Figure 4). Faults plotted as black lines.

4.2 The SAGENZ Network

The SAGENZ network was established in February 2000. At the time, the network more than doubled the number of Continuous GPS (CGPS) receivers from six[2] to 13. Although the project was designed for scientific purposes and covered a small geographical area, it

[2] By 2000, the number of existing CGPS sites operated by New Zealand agencies was six. These were Whagaperoa (AUCK), Chatham Island (CHAT), Wellington (WGTN), McQueens (MQZG), Hokitika (HOKI), and Dunedin (OUSD).

contributed significantly to the on going development of permanently operating GPS sites in New Zealand.

Since 2000, the SAGENZ network has increased from a total of seven receivers to ten. These receivers are operated in two modes: the first are sites that have permanent installations (CGPS) that telemeter the logged GPS data hourly to a local computer; the second mode utilizes three receivers that are regularly moved between five sites (semi-CGPS). The second mode of operation allows us to increase the spatial resolution of the project at the expense of not having a continuous data record.

The SAGENZ sites are shown in Figure 4. Four of the CGPS (QUAR, KARA, CNCL and NETT) have been operating since the start of the project. WAKA was initially a semi-CGPS site but in September 2002 it was upgraded to operate continuously. HORN was established

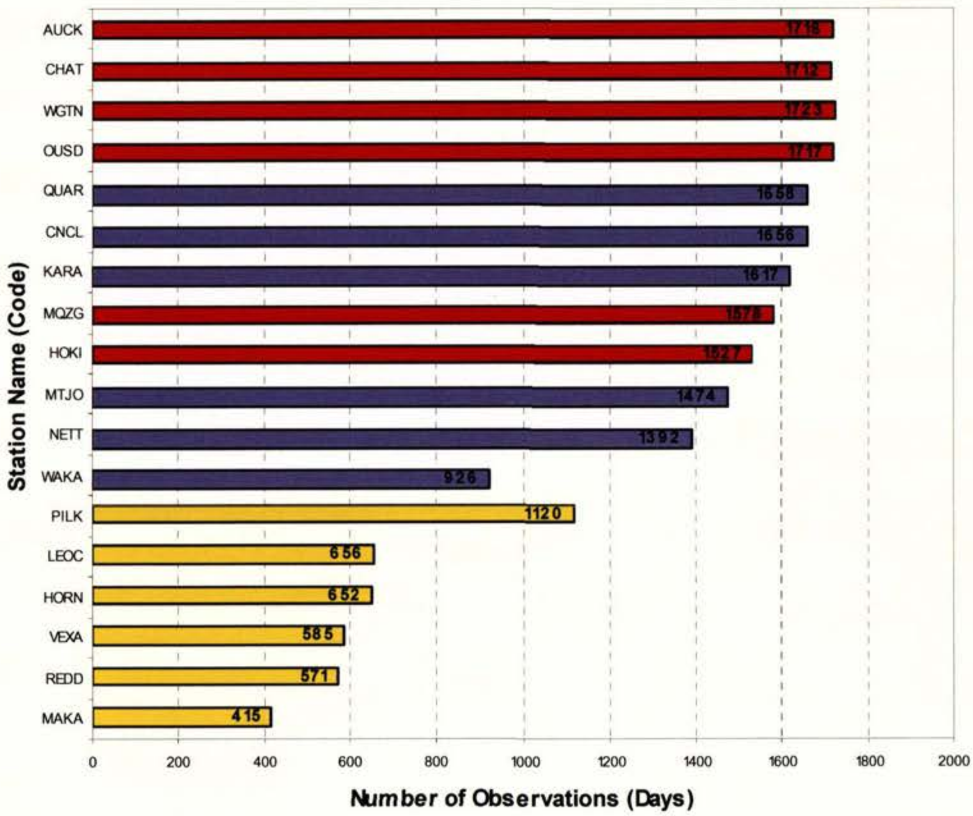

Figure 3: Total number of days with GPS data for both the SAGENZ sites (CGPS (blue), semi-CGPS (yellow)) and other New Zealand operated CGPS sites (red). The semi-CGPS sites have less than 700 observations days, while the CGPS sites that operate with few outages have in excess of 1500 observation days. The maximum number of observations since 1st January 2000 is 4.78 years × 365 = 1745 days.

as a CGPS site in November 2002. A seventh CGPS site, MTJO (Mt John, Lake Tekapo) located approximately 70km from the Alpine fault was established in August 2000 but has not been used in the strain analysis for this project.

The remaining 5 semi-CGPS sites (blue triangles) are located between the Alpine fault and the main divide. Ideally all sites would be operated as CGPS and the logged data download regularly. This has not been possible at some sites for two main reasons. The first is that it is difficult to establish a radio link to some of the sites owing to the topography and secondly, large quantities of snow during the winter making it difficult to keep some sites operational.

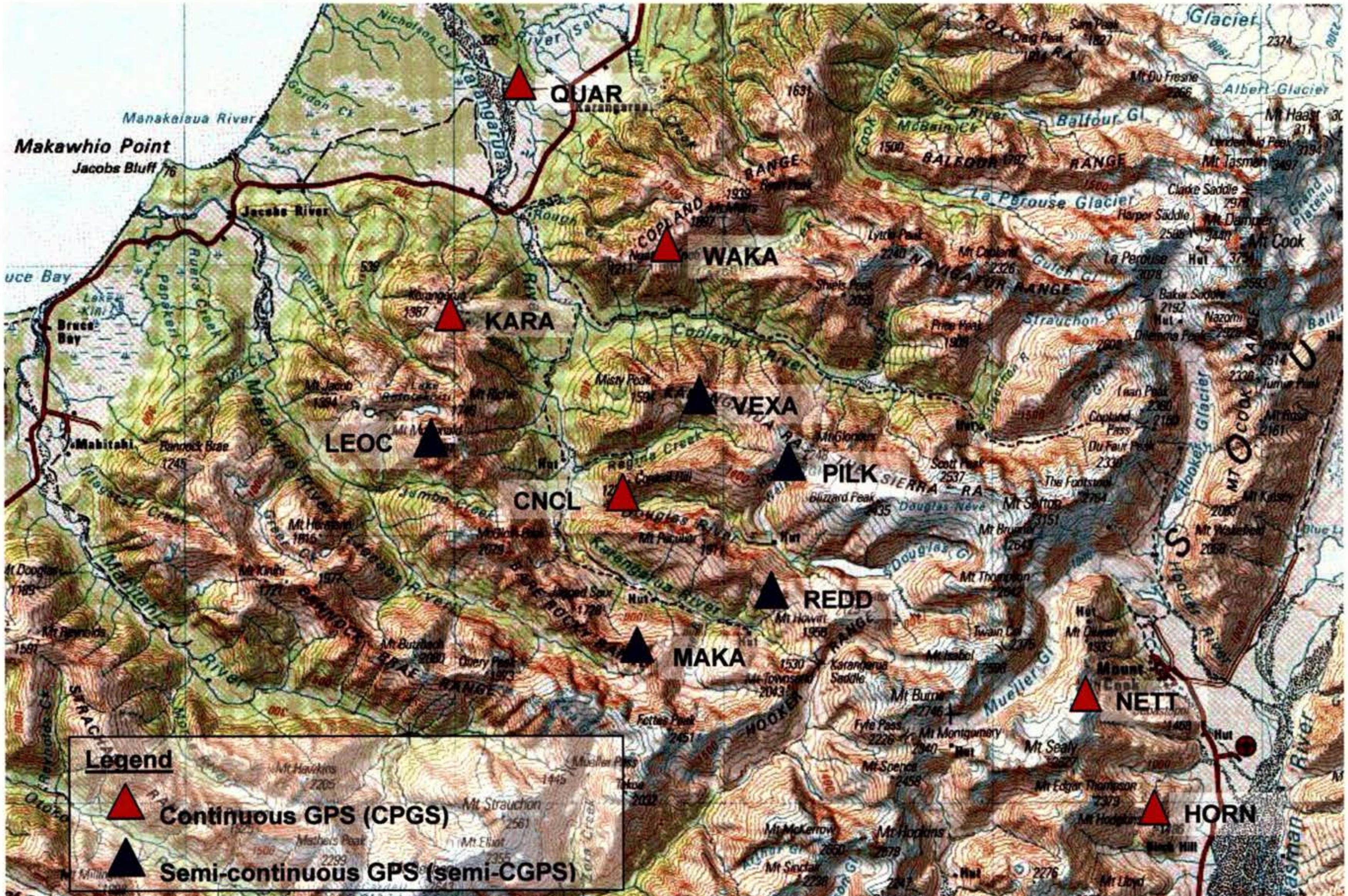

Figure 4: SAGENZ Network

4.2.1 GPS Equipment

Operating at each site is a dual frequency GPS receiver to measure and log GPS data collected through a geodetic dual frequency antenna (Figure 5). Each site is powered by a combination of five heavy duty batteries and four 80W solar panels.

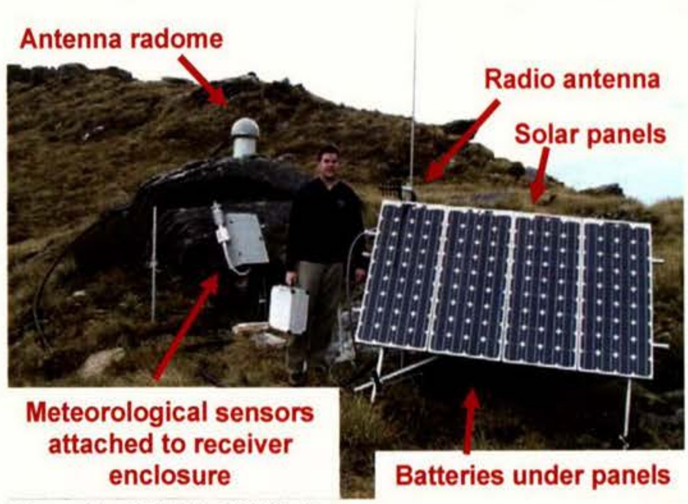

Figure 5: KARA CGPS site

The data is downloaded at the CGPS sites each hour using a radio telemetry link. A computer interrogates each CGPS site and "pulls" (transfers) the data from the receiver. The data is then sent via the internet to the Institute of Geological and Nuclear sciences (GNS) for dissemination and archiving. If the data link cannot be made, the data is stored on the receiver until a connection can be made. Each receiver can store 10 Mbytes of data, which corresponds to about 10-12 days of GPS observations, depending upon the sky visibility at a particular site.

Figure 6: VEXA Semi-CGPS site

Most of the CGPS sites also have a meteorological sensor that records the environmental pressure, temperature and relative humidity. Two sites do not have met sensors. At one site the sensor unit failed (CNCL in 2001) while at the second site the sensor was destroyed by snow (WAKA). (The sensor was actually damaged at MAKA during the winter, but the equipment was subsequently moved to WAKA.)

The semi-CGPS sites (Figure 6) are similar to the CGPS sites except that they do not have radio telemetry equipment, have two solar panels, three batteries and no metrological sensor. Having less equipment allows the site equipment to be transport easily between semi-CGPS sites via helicopter.

4.2.2 Monumentation

The SAGENZ sites have small monuments constructed using concrete and stainless steel reinforcing rods (Figure 7). (The only exception is MTJO (Mt John, Lake Tekapo), which is not used in the data analysis.) For stability, short pillars have been constructed, generally 300-400 mm high. A stainless steel plate with 5/8″ thread is set level into the top of the pillar.

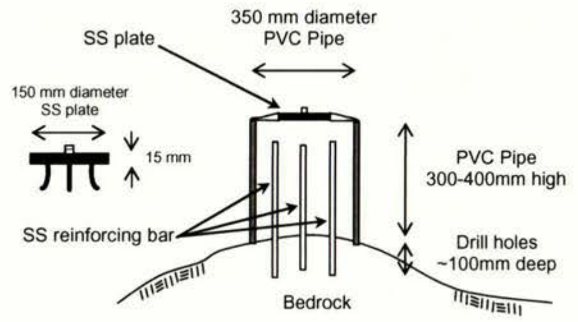

Figure 7: SAGENZ monuments. The PVC pipe is filled with concrete, poured directly onto the bedrock. Each monument has at least three, 12mm diameter, SS rods. The rods are fixed, with epoxy resin, into a hole drilled in the rock to a depth of 100mm. The SS plate, with a 5/8″ thread, is fixed to the concrete monument with three, 75mm long rods.

4.2.3 Observational Data

The continuity of the observed data is shown in Figure 8. The 12 sites at the top of the figure are the CGPS sites and provide a continuous data stream with only a few data outages. Data outages are generally caused by equipment failures (e.g. receiver, antenna, cables) but also

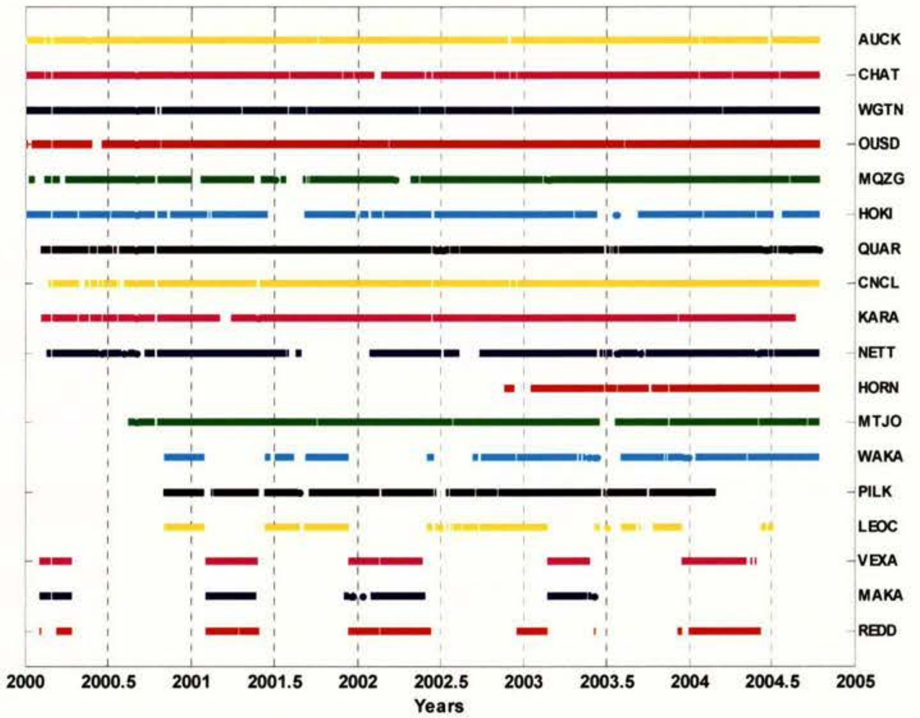

Figure 8: Data continuity from 1/1/2000 (DOY 1) to 15/10/2004 (DOY 289). SAGENZ sites have operated from since February 2000.

due to power failures. Environmental conditions such as short daylight hours and snow accumulation over a period of time does not allow the batteries to be charged adequately and therefore they slowly drain. For example, QUAR has several data outages during the middle of each year due to insufficient power that is in turn a combination of high topography (and vegetation) to the north and east of the site and low sun elevations. Located at an elevation of 2200 metres, NETT is significantly affected by snow and ice accumulating on the solar panels during the winter months that eventually prevents any available sun from recharging the batteries. It is then necessary to wait for the snow/ice to melt sufficiently before the equipment starts to operate again.

In contrast, PILK (1750 metres elevation) also receives significant quantities of snow but as the site is windy, the solar panels are generally kept clear of snow. It was the intention that this was a semi-CGPS site and therefore only occupied for six months each year. We had hoped to have occupied a sixth semi-CGPS site (MCKE), located at the base of the main divide, but between 2001 and 2003 there was too much snow to do this. However we did manage to collect data for three months over the summer in 2004.

WAKA was initially run as a semi-CGPS site until late 2002, before being upgraded to a CGPS site. The remaining sites have been operated as semi-CGPS.

4.3 Network Solution

A summary of the parameters estimated through the combined network solution is given in this section. This includes station velocities, position offsets caused by antenna changes and periodic terms that accounts for seasonal changes in the (horizontal) station positions.

4.3.1 Horizontal velocities

The horizontal velocities in a global reference frame, together with the seasonal variation terms, are estimated for each site (Table 3) and graphically shown in Figure 9. The stations are listed approximately west to east and so the gradual increase in the western velocity component (negative east velocity) and decrease in the northern velocity component can be seen.

	Station velocities		Station velocities relative to East coast fixed	
Station	**E ± σ (mm/yr)**	**N ± σ (mm/yr)**	**E ± σ (mm/yr)**	**N ± σ (mm/yr)**
HOKI	-6.2 ± 0.93	42.0 ± 0.99	30.6 ± 0.93	11.2 ± 0.99
QUAR	-10.8 ± 0.93	41.7 ± 0.97	26.0 ± 0.93	10.9 ± 0.97
KARA	-13.9 ± 0.93	40.9 ± 0.97	22.9 ± 0.93	10.1 ± 0.97
LEOC	-15.4 ± 0.93	37.2 ± 0.97	21.4 ± 0.93	6.3 ± 0.97
WAKA	-16.0 ± 0.93	40.1 ± 0.98	20.8 ± 0.93	9.3 ± 0.98
VEXA	-18.6 ± 0.93	37.6 ± 0.98	18.2 ± 0.93	6.8 ± 0.98
CNCL	-19.2 ± 0.93	37.5 ± 0.97	17.6 ± 0.93	6.6 ± 0.97
MAKA	-21.0 ± 0.93	36.6 ± 0.98	17.1 ± 0.93	6.3 ± 0.98
PILK	-19.7 ± 0.93	37.1 ± 0.98	15.8 ± 0.93	5.8 ± 0.98
REDD	-22.0 ± 0.93	36.4 ± 0.98	14.8 ± 0.93	5.5 ± 0.98
NETT	-23.9 ± 0.94	34.3 ± 0.99	12.9 ± 0.94	3.5 ± 0.99
HORN	-26.2 ± 0.94	32.1 ± 1.00	10.5 ± 0.94	1.3 ± 1.00
MTJO	-31.1 ± 0.93	31.6 ± 0.98	5.7 ± 0.93	0.8 ± 0.98
MQZG	-36.8 ± 0.93	30.8 ± 1.02	0.0 ± 0.93	0.0 ± 1.02
OUSD	-34.3 ± 0.95	31.2 ± 0.98	2.5 ± 0.95	0.4 ± 0.98

Table 3: Station velocities are with respect to the nominal (global) IGS station velocities. Relative velocities (right hand side) are computed holding MQZG fixed (East coast fixed). One sigma standard errors.

These differences in velocity (or velocity gradient) imply strain acculmulation in the Southern Alps. Most of the deformation is occouring in the 70km wide zone between MTJO (Lake Tekapo) and QUAR. Over this distance, the difference in velocity (and hence rate of strain) is

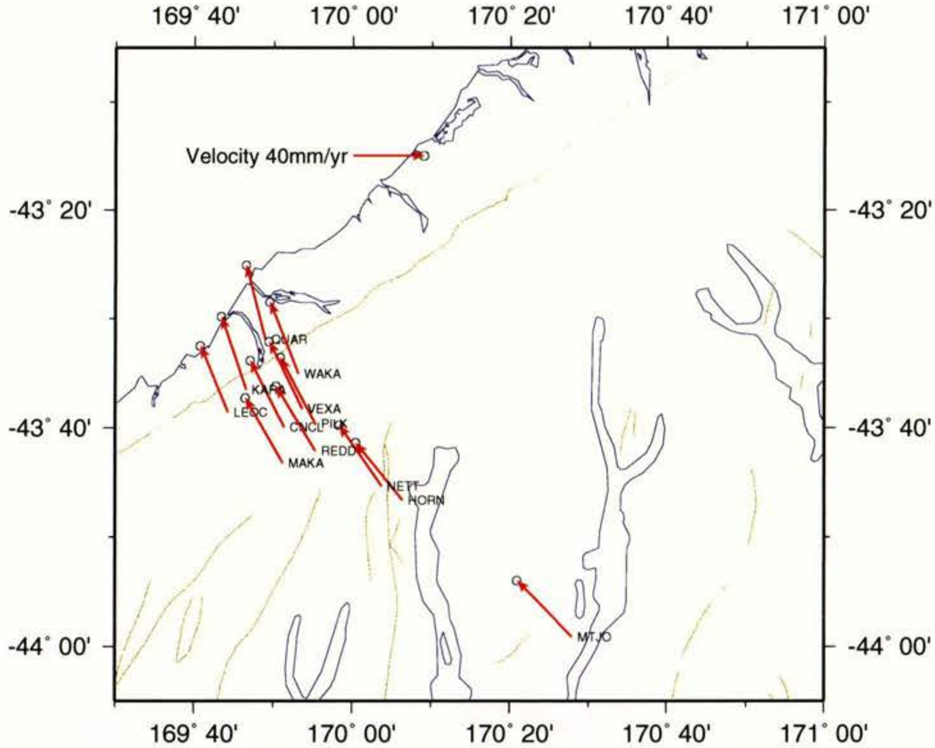

Figure 9: SAGENZ network station velocities with respect to global IGS station velocities. (95% confidence error ellipse). Approximate location of major fault lines indicated by light green lines.

22mm/yr. As shown in Figure 10, the motion with respect to the east coast of the South Island has a predominatly strike-slip componemt parallel with the Alpine fault.

Also clearly seen in Figure 10 is the velocity gradient across this zone (approximately 30km).

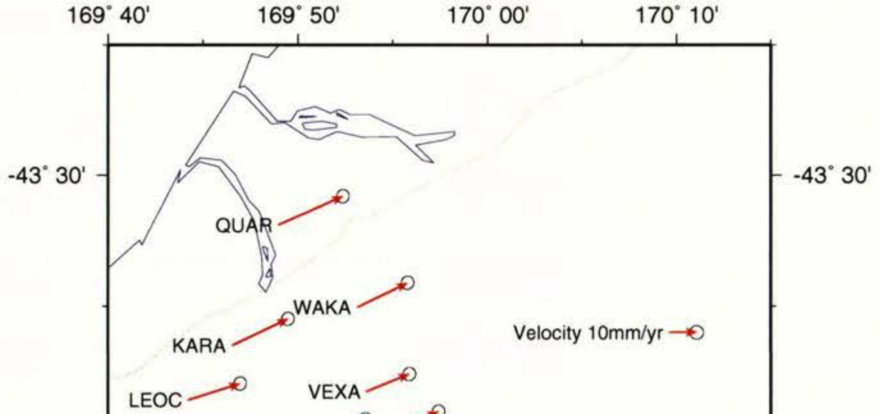

Figure 10: SAGENZ network velocities relative to the East coast fixed (MQZG) (95% confidence error ellipse). Approximate location of major fault lines indicated by light green lines.

There is a consistent increase in the strike-slip parallel component from 13mm/yr at NETT to 26mm/yr at QUAR. The velocity direction at NETT appears to be consistent with the other sites in the SAGENZ network, but the velocity direction at HORN appears be slightly inconsistent. Although HORN has nearly two years of data and we expect the horizontal velocity to be well determined, the data period may be still too short. It could also be caused by localised deformation, which would also become more evident with more data.

4.3.2 Antenna Offsets

Inevitably equipment changes are necessary, most often due to component failures. Although most equipment changes do not affect the collected data substantially or data quality, a change in the antenna can potentially change the geometrical relationship between the antenna and antenna mount (pillar), known as the antenna offset or antenna phase variation. The reason for this is that the antenna electrical centre does not coincide with the geometrical centre of the antenna and it is well established that the offset changes with both satellite elevation (dominant effect) and satellite azimuth (minor effect). Even though the antennas are calibrated it is difficult to accurately determine antenna phase variations and other effects such as the aging of the antenna electronic components is not well understood.

Changes caused by antenna phase variation can often be seen when one type of antenna is exchanged for another. This is especially true when an antenna made by one manufacturer is exchanged for an antenna made by a second manufacturer. For this reason we have tried to maintain the same type of antenna through-out the SAGENZ network. This was the Trimble manufactured Dorne Margolin antenna with chokerings (IGS code TRM29659.00). In addition, for the semi-CGPS sites, we have also tried to use the same antenna at the same sites when the equipment has been moved.

However, using the same type of antenna consistently has not always been possible. By the time the CGPS site HORN was installed in late 2002, antenna design had changed (and hopefully improved) and this site used the new type of antenna, namely, the Trimble Zehpyr Geodetic (IGS code TRM41249.00).

		Antenna changed from		Antenna changed to		
Station	Date	Serial Number	Antenna Type	Serial Number	Antenna Type	Reason
MQZG	2001.669	148020	TRM29659.00	905	ASH701945C_M	Equipment upgrade
HOKI	2003.680	573	ASH700936D_M	11885765	TRM41249.00	Equipment upgrade
CNCL	2000.592	67548	TRM29659.00	63995	TRM29659.00	Antenna failed
MAKA	2001.077	73538	TRM29659.00	67548	TRM29659.00	Equipment change
MAKA	2003.000	67548	TRM29659.00	73538	TRM29659.00	Equipment change
WAKA	2002.406	67545	TRM29659.00	67548	TRM29659.00	Change to CGPS

Table 4: Antenna type changes. Note that the sites MQZG and HOKI are not part of the SAGENZ network.

Station	Date	ΔE (mm)	ΔN (mm)	ΔH (mm)	Network
MQZG	2001.669	-2.4 ± 0.2	0.3 ± 0.2	-13.1 ± 0.8	Regional
HOKI	2003.680	1.7 ± 0.2	1.1 ± 0.3	9.8 ± 1.0	Regional
CNCL	2000.592	0.4 ± 0.4	-1.5 ± 0.3	4.6 ± 1.3	SAGENZ CGPS
MAKA	2001.077	1.7 ± 0.6	1.7 ± 0.5	-6.3 ± 2.0	SAGENZ semi-CGPS
MAKA	2003.000	-0.2 ± 0.6	2.8 ± 0.5	0.0 ± 2.0	SAGENZ semi-CGPS
WAKA	2002.406	0.8 ± 0.5	0.4 ± 1.2	-2.2 ± 1.6	SAGENZsemi-CGPS/CGPS

Table 5: Estimated antenna offsets.

Table 4 and Table 5 list the antenna changes and estimate antenna offsets respectively (also reported in Beavan (2004)). In addition to antenna changes at three of the SAGENZ sites (CNCL, MAKA, WAKA), the antennas types at two antennas have changes at two regional CGPS sites (HOKI and MQZG). At MQZG, the antenna type changed from a Trimble to an Ashtech (TRM29659.00 → ASH701945C_M), and at HOKI the change was from an Ashtech to a Trimble (ASH700936D_M → TRM41249.00). For each site the change is between the same manufacturers but opposite direction, and although the antenna models are not identical, the estimated offsets are similar but of opposite sign.

Nominally the TRM29659.00, ASH701945C_M and ASH700936D_M have identical antenna elements known as the Dorne Margolin (with chokerings), (but in practice this is not the case), while the TRM41249.00 (Zephyr Geodetic antenna with Ground Plane) is a more recently developed antenna. The measured east offset is approximately -2 and +2mm (significant at the 95% confidence interval), and the height offset of -13 and +10mm (also significant at the 95% confidence level). The north offset is not significant at the 95% confidence level. The antenna offsets given here are similar to those reported in (Beavan *et al.* 2004)

This demonstrates the potential problem when there are changes in the antenna types and for this reason we have endeavoured to maintain the same type of antenna. The estimated offsets at the three SAGENZ sites (Table 5) are generally small (horizontal offsets less than 2mm), for which some of the offset may be caused by systematic variations in the data, (for example seasonal effects), than actual changes due to differences between antennas. In addition, it is more difficult to estimate the antenna offsets at semi-CGPS sites owing to the substantial data gaps (see also Figure 8). This is especially true for MAKA as this station has only been occupied as a semi-CGPS site, and also for WAKA which has only operated continuously since the antenna change.

For this project, the important aspect is that the largest antenna offsets affect the vertical component. They therefore will not significantly affect velocity and or strain parameter estimates. The horizontal component offsets are at the ±0-2mm level and similar to the horizontal position noise level (see also Section 4.3.3).

4.3.3 Horizontal time series

In this section the quality of the station positions derived from the GPS data is examined. Table 6 gives, for each site, the coordinate component repeatability in terms of the rms for the east and north components with overall mean rms values of ±2.0mm and ±1.7mm respectively. Clearly the station with the worst repeatability is NETT, most likely due to periodic build up of snow and ice on the antenna radome. If NETT is removed, the mean rms of both the east and north components reduce to ±1.6mm.

As an example, Figure 11 shows the horizontal time series of the east and north coordinates and a horizontal plot for station QUAR. There is a small but obvious cyclical pattern in both coordinate components. The amplitude is approximately 1mm. All of the SAGENZ sites exhibit cyclical patterns that are most likely to be caused by changing environmental conditions during the year, and may influence multipath characteristics around the antenna environment. Antenna multipath has not been investigated.

Although the sites exhibit similar cyclical trends, all sites behave differently. A comparison of the time series plots for QUAR, CNCL and KARA (Figure 11-Figure 13) demonstrates that the coordinate components of each site have different characteristics. For example, the northing component for KARA is more erratic than CNCL. There appears to be a period of strong westward movement (negative east) in the spring to early summer at CNCL in late 2001 and 2003 (and possibly the start of a similar trend in 2004). The same motions do not occur at KARA.

Station	Observations	E (mm)	N (mm)
WGTN	1723	2.2	1.6
OUSD	1717	1.8	1.7
AUCK	1716	1.6	1.8
CHAT	1712	2.3	2.2
QUAR	1658	1.4	1.3
CNCL	1656	1.8	1.1
KARA	1617	1.7	1.6
MQZG	1578	1.3	1.6
HOKI	1527	1.2	1.3
MTJO	1474	1.3	1.1
NETT	1392	8.5	3.2
PILK	1120	1.8	1.7
WAKA	926	1.7	2.7
LEOC	656	1.5	2.2
HORN	652	1.9	1.6
VEXA	585	1.0	1.4
REDD	571	1.3	1.1
MAKA	415	1.0	1.1
Mean		**2.0**	**1.7**

Table 6: Total number of site positions (observations) and coordinate component repeatability (rms) of GPS sites

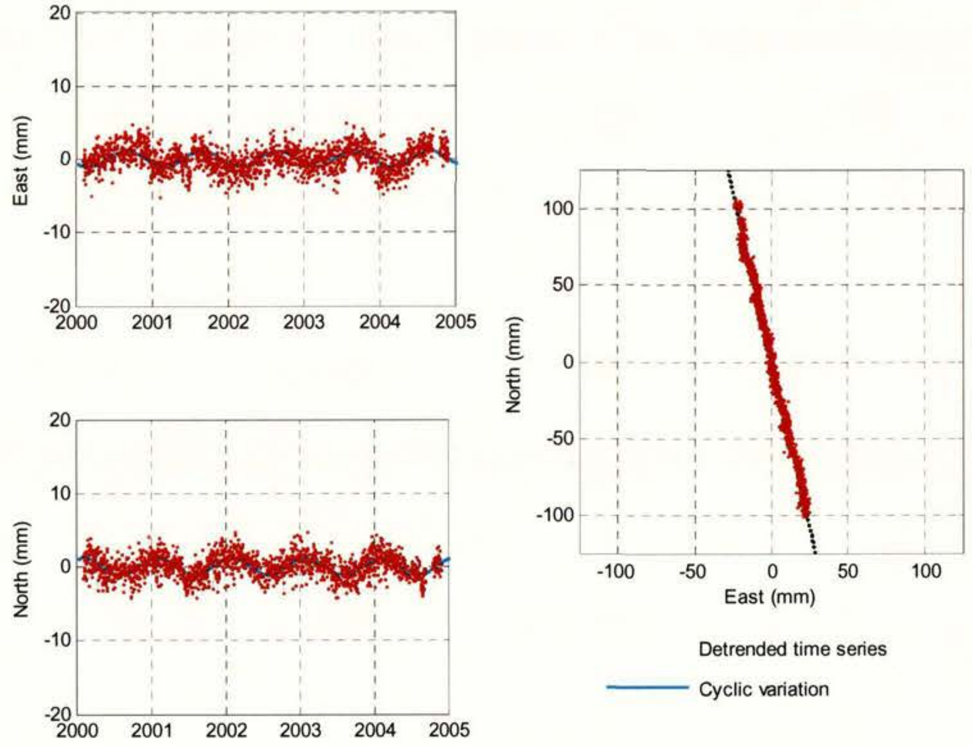

Figure 11: Time series and horizontal plot for QUAR. Local reference frame (East and North)

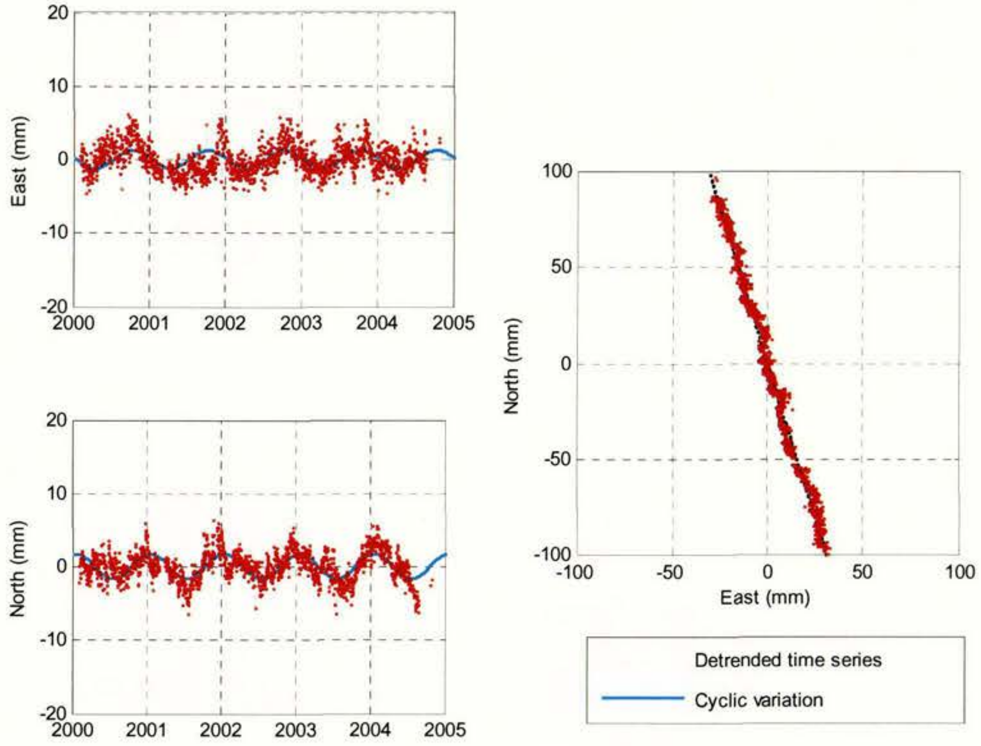

Figure 12: Time series and horizontal plot for KARA. Local reference frame (East and North)

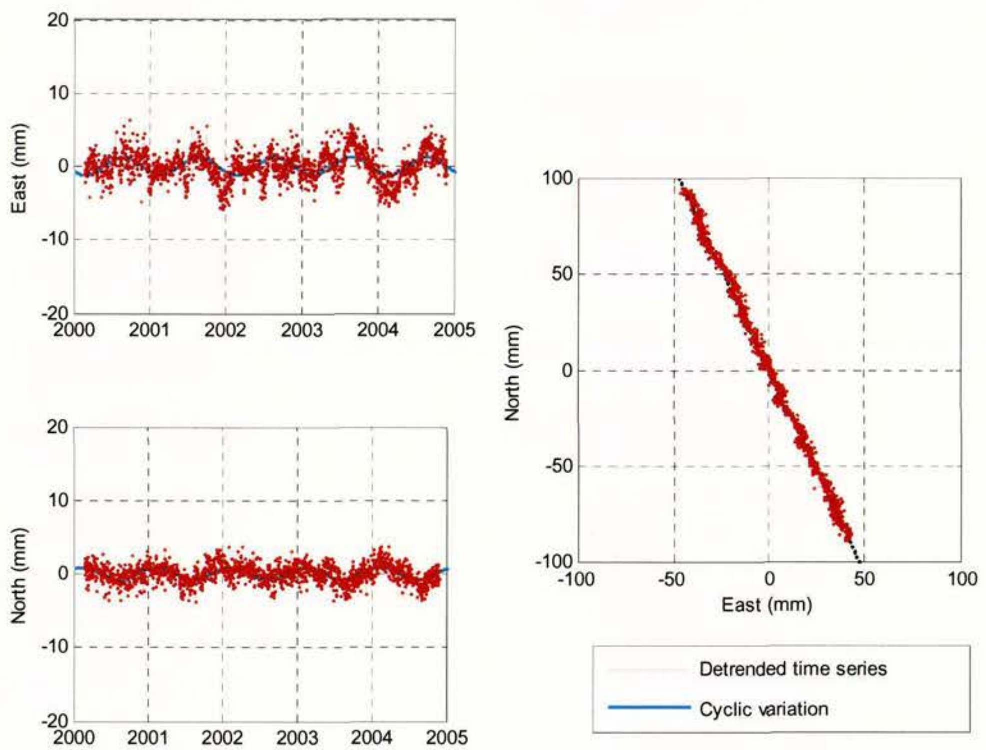

Figure 13: Time series and horizontal plot for CNCL. Local reference frame (East and North)

4.3.4 Seasonal terms

Cyclical patterns can be seen at both semi-CGPS and CGPS sites. For most sites the estimated cyclical terms are small (amplitude less than 1-2mm), but at other sites the displacements are large enough to be significantly. For the SAGENZ network, the magnitude of the cyclical patterns was an unexpected result (Denys *et al.* 2003; Beavan *et al.* 2004). One of the best examples is at PILK (Figure 14). The estimated amplitudes of the annual terms are 6mm and 3mm for the east and north components respectively. The cyclic variation is not symmetrical with a faster west and south motion during spring to early summer. To account for this, a semi-annual (6 month) term is included.

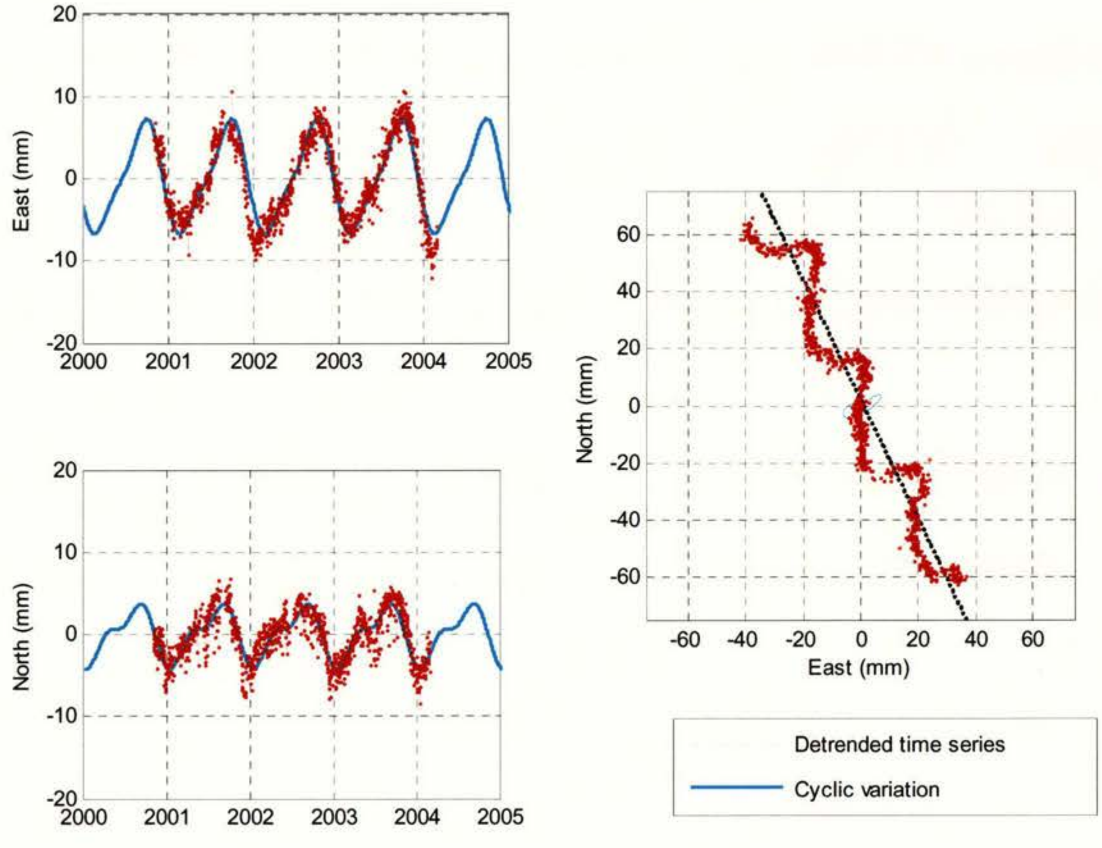

Figure 14: Time series and horizontal plot for PILK. Local reference frame (East and North)

The amplitude and phase terms are given in Table 7 and Table 8 respectively. The sites are listed from west (HOKI, QUAR) to east (MQZG, OUSD). Most sites have small amplitudes of less than 2mm. The three sites with large periodic terms are PILK, NETT and WAKA. The other feature to note is that the phase of the east component for the nine sites west of the main divide (QUAR, KARA, LEOC, WAKA, VEXA, CNCL, PILK, MAKA, REDD) is similar with a mean value of -159° (200°). In contrast, the mean of the phase (east component) of the two sites immediately east of the main divide (NETT, HORN) is 5°; but of opposite sign to the sites to the west. The phase of these two groups is very nearly 180° indicating that the cyclical trends of these sites are opposite or out of phase.

There is also the possibility that there are further regional groups of the SAGENZ sites. KARA and LEOC are the two south-western most sites and the phase of both of these sites are similar and the most negative (mean -190°). The phase of the four central sites (QUAR, VEXA, WAKA, CNCL) are closely grouped together with the phase range between -139° to -157° (203°-221°).

Similar patterns for the north phase component are not so obvious.

	Amplitude Annual Term		Amplitude Semi-annual Term	
Station	**E ± σ (mm)**	**N ± σ (mm)**	**E ± σ (mm)**	**N ± σ (mm)**
HOKI	0.5 ± 0.05	0.5 ± 0.05		
QUAR	1.1 ± 0.05	1.1 ± 0.05		
KARA	1.2 ± 0.06	1.7 ± 0.06		
LEOC	2.0 ± 0.12	1.0 ± 0.12		
WAKA	**3.3 ± 0.08**	**3.3 ± 0.13**		
VEXA	1.3 ± 0.18	1.9 ± 0.21		
CNCL	1.2 ± 0.06	0.9 ± 0.04		
PILK	**6.4 ± 0.08**	**3.2 ± 0.07**	**1.6 ± 0.08**	**1.5 ± 0.07**
MAKA	0.7 ± 0.17	1.1 ± 0.21		
REDD	0.8 ± 0.19	0.7 ± 0.11		
NETT	**17.7 ± 0.34**	**4.7 ± 0.13**	**5.6 ± 0.32**	**0.6 ± 0.13**
HORN	0.6 ± 0.11	0.5 ± 0.09		
MTJO	0.5 ± 0.05	0.2 ± 0.04		
MQZG	0.1 ± 0.04	0.0 ± 0.06		
OUSD	0.7 ± 0.06	0.1 ± 0.06		

Table 8: Amplitude annual and semi-annual terms

	Phase Annual Term		Phase Semi-annual Term	
Station	**E ± σ (°)**	**N ± σ (°)**	**E ± σ (mm)**	**N ± σ (°)**
HOKI	-136 ± 5	73 ± 6		
QUAR	-148 ± 3	58 ± 2		
KARA	-194 ± 3	72 ± 2		
LEOC	-186 ± 2	-73 ± 10		
WAKA	-159 ± 1	-104 ± 2		
VEXA	-140 ± 4	-12 ± 5		
CNCL	-145 ± 3	46 ± 3		
PILK	-161 ± 1	-124 ± 1	-128 ± 3	-89 ± 3
MAKA	-130 ± 11	178 ± 6		
REDD	-169 ± 6	142 ± 13		
NETT	2 ± 1	-139 ± 2	41 ± 3	145 ± 12
HORN	7 ± 11	148 ± 11		
MTJO	-160 ± 5	76 ± 10		
MQZG	154 ± 40	-50 ± 99		
OUSD	97 ± 5	-121 ± 35		

Table 7: Phase annual and semi-annual terms. Phase is referenced to 1st January, so a phase of zero corresponds to the start of the sinusoidal oscillation.

The geophysical reasons for these cyclical station position displacements are not understood at this stage, but it is likely to be caused by a combination of snow and ice mass loading, rock porosity and the orientation of the topography. See Section 5.3.

5 Network Strain Analysis

This section investigates the estimated long term geodetic strain rates. Initially, the (Alpine) fault parallel and normal velocities are given and compared with the values used in Beavan *et al.* (1999). Using data from both the CSI and SAGENZ networks, groups of stations covering regions (or sub networks) are used to compare the long term strain rates. The SAGENZ network can be subdivided into smaller groups of stations that allows a better overview of how the region is deforming, or more particularly, which areas are deforming differently. Strain rates are also derived for baseline extension or contraction between adjacent stations.

5.1 Alpine Fault Parallel and Normal Velocities

A comparison of the velocities normal and parallel to the strike of the Alpine fault can be made between the SAGENZ network and the values used in the dislocation model determined by Beavan *et al.* (1999). The velocities used are from their Model 5, which constrains two fault planes to meet (Beavan *et al.* 1999, Figure 12). This is probably the most geologically reasonable model. (An updated model is given in (Beavan *et al.* 2004).) The SAGENZ velocities are resolved into fault parallel and fault normal velocities based on an average Alpine fault surface trace of 54.8°. The fault parallel and normal velocities and the velocity differences are given in Table 9.

Overall the agreement between Beavan *et al.* (1999) and the SAGENZ velocities is surprisingly good. The precision of the SAGENZ velocities are approximately half (50% better) compared to Beavan *et al.* (1999) (see Table 3). For the fault normal component, only one site has a difference of more than 1 mm/year (LEOC). For the fault parallel component, QUAR, KARA, LEOC, WAKA and HORN (5 sites) have velocity differences greater than 1 mm/year. The SAGENZ velocities are all smaller than those determined by Beavan *et al.* (1999). Some of this difference could be attributed to different velocities used to determine the East Coast fixed reference frame. (SAGENZ used a single site MQZG (Southern Banks Peninsular), Beavan *et al.* (1999) averaged several sites in mid-Canterbury.)

The fault parallel and fault normal components are shown in Figure 15 for the profile between HOKI (-19km) and MTJO (70km). Even with several large gaps between sites, the overall velocity gradient in both the parallel and normal velocities is apparent. Also obvious is the abnormal behaviour at LEOC, which shows as a sharp jump in both the parallel and normal velocity components. The position time series for the site shows a significant seasonal cycle. As the site has only been occupied during the winter months, the whole of the cycle has not been well determined and may therefore be contributing to a bias in the velocity estimate.

The fault parallel gradient between NETT and HORN also appears to be incorrect. At this stage it is difficult to determine which station has caused the inconsistency, (or both).

		Velocities relative to East coast fixed		Velocities from Beavan *et al.* (1999)		Difference (SAGENZ minus Beavan *et al.* (1999))	
site	Distance (km)	Normal (mm/yr)	Parallel (mm/yr)	Normal (mm/yr)	Parallel (mm/yr)	Normal (mm/yr)	Parallel (mm/yr)
HOKI	-19	8.4	31.4				
QUAR	-3.2	6.0	27.5	6.6	30.7	-0.6	**-3.2**
KARA	2.2	4.9	24.5	4.8	26.3	0.0	**-1.8**
LEOC	3.7	7.1	21.2	4.8	25.7	**2.3**	**-4.6**
WAKA	4.8	4.3	22.3	4.3	23.7	0.0	**-1.4**
VEXA	10.1	4.9	18.8	4.8	19.3	0.1	-0.5
CNCL	11.1	4.7	18.2	4.9	18.6	-0.3	-0.3
MAKA	13.5	4.7	17.6	4.8	16.9	-0.1	0.8
PILK	16.1	4.3	16.2	4.7	16.0	-0.3	0.2
REDD	17.3	3.9	15.3	4.5	15.1	-0.5	0.1
NETT	28.5	4.6	12.6	4.4	13.1	0.2	-0.6
HORN	32.5	5.0	9.3	4.4	12.3	0.6	**-3.0**
MTJO	68	2.7	5.1	2.5	5.7	0.2	-0.6
MQZG	141	0.0	0.0				
OUSD	244	1.1	2.3				

Table 9: Fault parallel and normal velocities for the SAGENZ network and from Beavan *et al.* (1999). The velocities are relative to holding MQZG fixed (East Coast fixed) and resolved using an average strike for the Alpine fault of 54.8°.

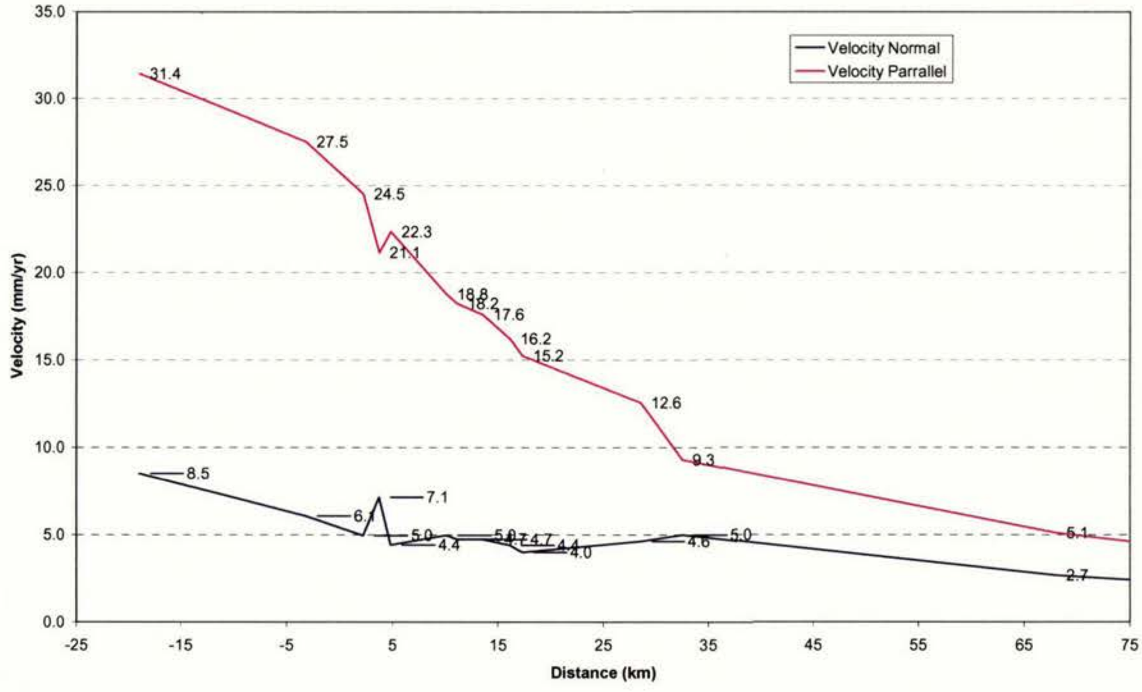

Figure 15: Fault parallel and normal velocities for the SAGENZ network. The velocities are relative to holding MQZG fixed (East Coast fixed) and rotated using an average strike for the Alpine fault of 54.8° Distance 0km is the location of the Alpine fault.

5.2 Baseline Length Change

A direct measurement and graphical plot of the deformation in the SAGENZ network stations can be determined from the change in baseline length. The baseline length is the distance computed between the (horizontal) site coordinates and hence is determined for pairs of sites. Using both the CGPS and semi-CGPS sites, a time plot of the change in baseline length shows systematic decrease/increase over time. Even when GPS data is missing, due to either equipment failures or the re-location of the semi-CGPS equipment, the changes in baseline length can be demonstrated.

5.2.1 Baseline contraction

Table 10 lists the baselines in the SAGENZ network for which the distance is shortening (contraction). Sites that have been operated continuously (e.g. KARA, CNCL) or have long occupations (e.g. PILK), have in excess of 1300 distance measurements. Several of the semi-CGPS sites have only a small number of days (e.g. <300) or insufficient data to determine a reliable change in baseline length e.g. the baseline MAKA-LEOC has only 11 observations.

From	To	Velocity (mm/yr)	se (+/-)	Distance (km)	Length Change (ppm/yr)	t	rms (+/-)	Obs
CNCL	LEOC	-3.7	0.11	9.95	-0.37	3.4	2.8	650
KARA	VEXA	-3.4	0.05	10.07	-0.34	6.8	1.4	556
KARA	WAKA	-2.9	0.09	9.30	-0.31	3.4	2.7	870
QUAR	WAKA	-2.5	0.07	8.09	-0.31	4.4	2.1	899
REDD	CNCL	-1.0	0.05	6.59	-0.16	3.2	1.4	564
KARA	CNCL	-1.4	0.04	9.15	-0.15	3.8	1.9	1576
VEXA	PILK	-0.4	0.04	3.42	-0.13	3.3	1.3	585
NETT	PILK	-1.9	0.15	15.47	-0.12	0.8	7.4	1385
NETT	REDD	-0.9	0.20	12.79	-0.07	0.4	5.3	518
NETT	MAKA	-4.2	0.20	17.27	-0.24	1.2	3.7	382
HORN	WAKA	-1.2	0.23	27.87	-0.04	0.2	2.6	551
HORN	REDD	-1.0	0.52	17.05	-0.06	0.1	2.7	212
NETT	MAKA	-4.2	0.20	17.27	-0.25	1.3	3.7	382
NETT	PILK	-1.9	0.15	15.47	-0.12	0.8	7.4	1385
NETT	KARA	-4.7	0.18	28.31	-0.17	0.9	8.9	1304
NETT	CNCL	-2.9	0.19	19.33	-0.15	0.8	9.6	1350
NETT	REDD	-0.8	0.23	12.79	-0.06	0.3	6.3	518
HORN	KARA	-4.8	0.20	32.58	-0.15	0.8	2.2	598
HORN	REDD	-1.0	0.52	17.05	-0.06	0.1	2.7	212
REDD	MAKA	-0.9	0.12	5.90	-0.16	1.3	1.3	272
WAKA	VEXA	-0.3	0.23	6.00	-0.05	0.2	1.5	213
WAKA	HORN	-1.2	0.23	27.87	-0.04	0.2	2.6	551

Table 10: Distance contraction of selected baselines.

The velocity and velocity precision (standard error), in millimetres per year, is computed by regression on the baseline distance after correction for seasonal biases. The rate of length change is thus computed by

$$\delta \dot{l}\ (ppm / year) = \frac{v\ (mm / yr)}{d\ (km)}$$

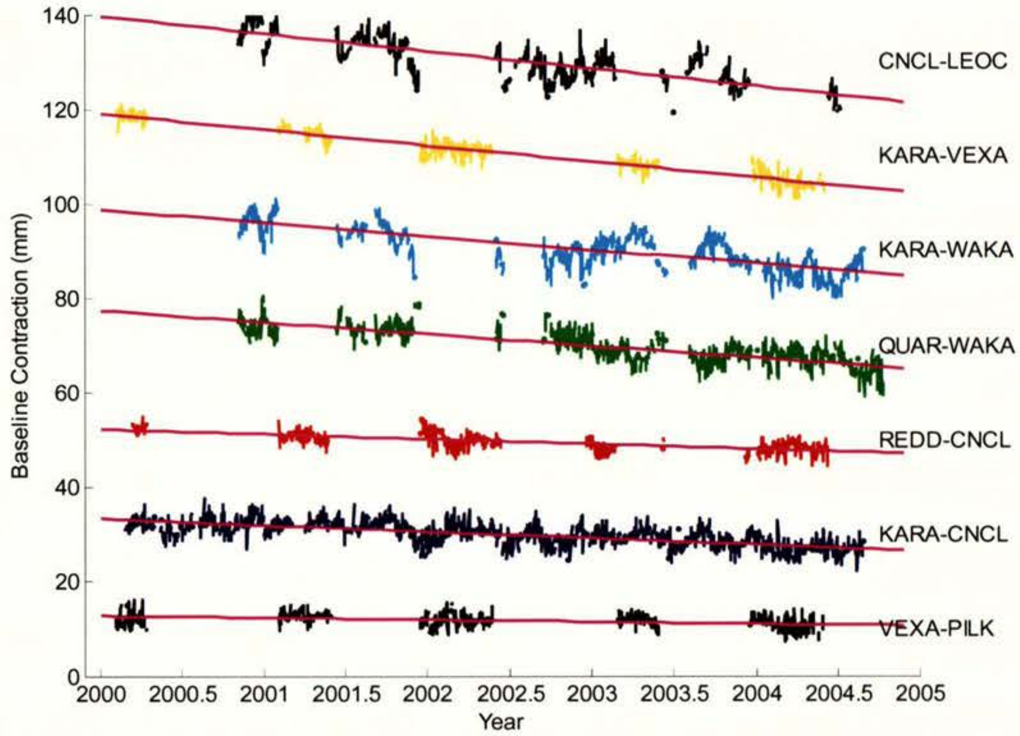

Figure 16: Baseline length contraction

To determine if the change in length of each baseline is significant or not, an approximate student-t statistic is computed using the length change and assuming that the velocity standard

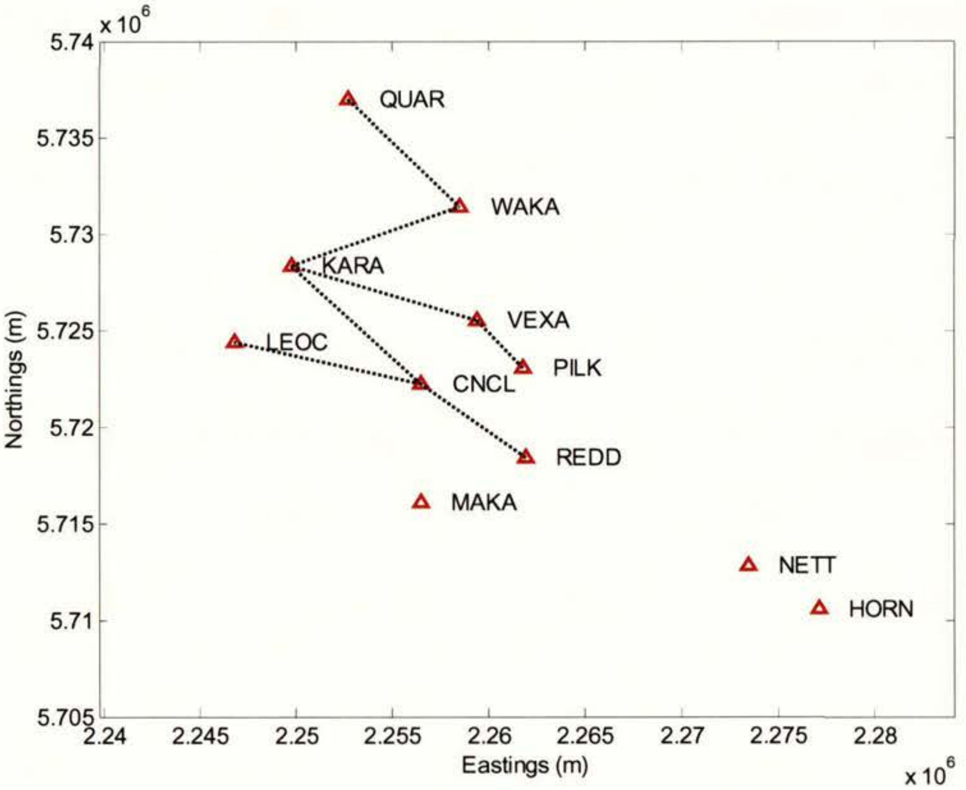

Figure 17: Map of the baselines that have significant length contraction

error equals the baseline length change standard error. That is

$$t \text{ statistic} = \frac{\delta \dot{l}}{\sigma_v} = \frac{\delta \dot{l}}{\sigma_{\dot{\varepsilon}}}$$

This is not strictly correct as the degrees of freedom have not been taken into account, but the statistic does give a means of ordering the estimated baseline strain estimates. The first 7 lines in Table 10 are the baselines with significant baseline contraction based on a critical t value of greater than 3. These baselines are plotted in Figure 16. As also shown for the long term strain estimates (Section 5.3.1), these are largely east-west orientated baselines. It also reinforces the result in Section 5.3.3 that the maximum contraction rate is on the western side of the profile (trace of the Alpine fault).

5.2.2 Baseline extension

The same tabulation and figures are given for the baseline length extension as was done for the baseline contraction. The lines are ordered using the t-statistic (Table 11).

From	To	Velocity (mm/yr)	se (+/-)	Distance (km)	Length Change (ppm/yr)	t	rms (+/-)	Obs
LEOC	KARA	4.1	0.11	4.94	0.83	7.5	2.7	651
LEOC	QUAR	6.1	0.09	13.92	0.44	4.9	2.2	636
PILK	REDD	1.7	0.08	4.61	0.37	4.6	2.4	571
KARA	QUAR	1.8	0.04	9.13	0.20	5.0	2.0	1576
CNCL	QUAR	2.4	0.03	15.30	0.15	5.0	1.5	1610
CNCL	VEXA	0.7	0.05	4.37	0.15	3.0	1.5	563
CNCL	MAKA	0.5	0.06	6.07	0.09	1.5	1.2	397
PILK	WAKA	0.7	0.08	8.99	0.08	1.0	2.5	925
PILK	CNCL	0.2	0.06	5.34	0.04	0.7	3.0	1651
PILK	HORN	0.8	0.20	19.70	0.04	0.2	2.3	645
HORN	PILK	0.8	0.20	19.70	0.04	0.2	2.3	645
NETT	WAKA	0.3	0.20	23.81	0.01	0.1	5.4	766

Table 11: Distance extension of selected baselines

Six baselines have a significant extension. The lines are plotted in Figure 18. The lines with significant extension generally have a north-south orientation. Note that two of the lines include LEOC exhibit significant extension. As pointed out in Section 5.1 (and also Section 5.3.3), it is likely that the inconsistent velocity at this site will be producing this effect.

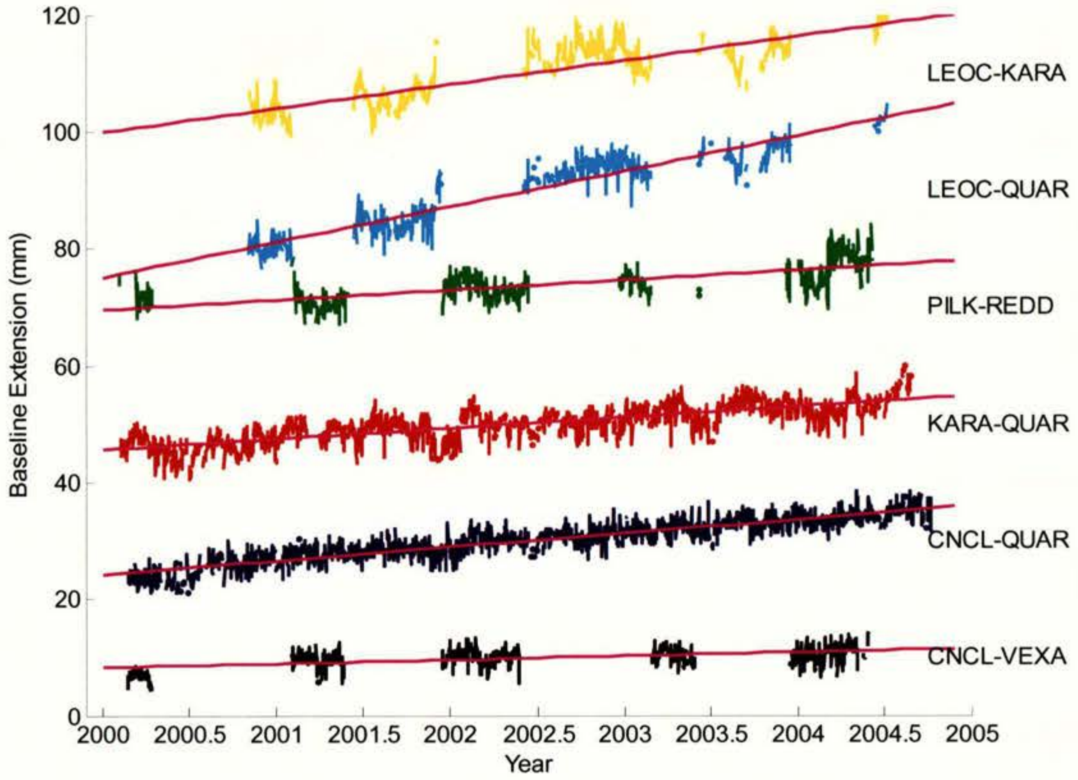

Figure 18: Baseline length extension

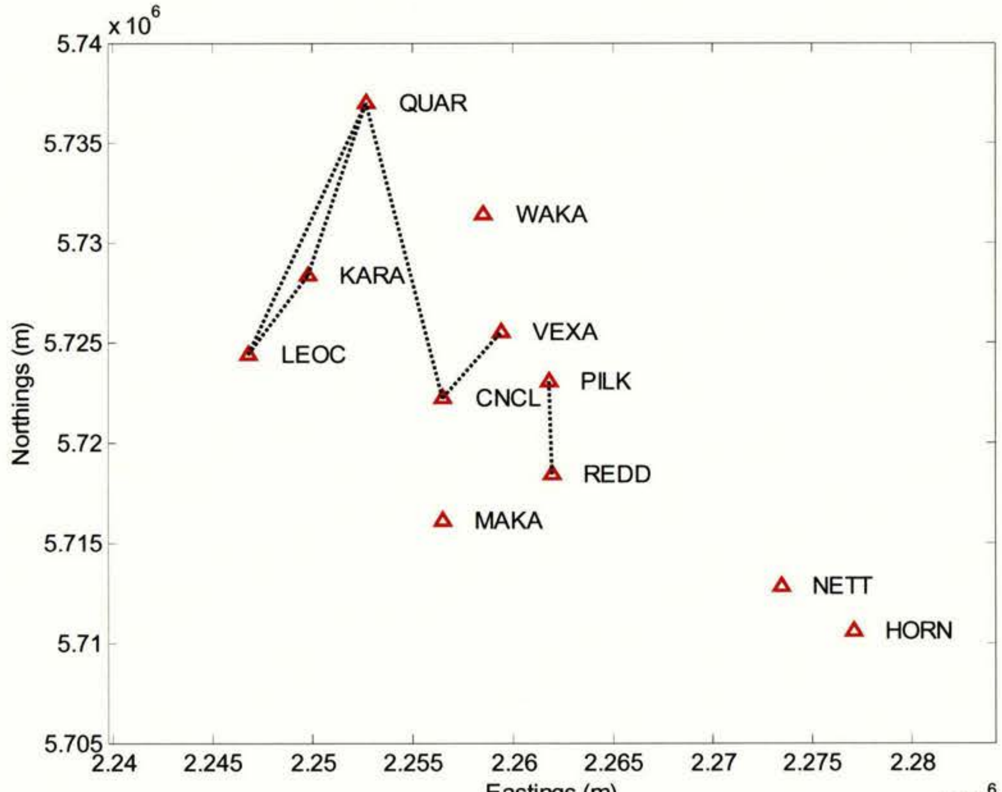

Figure 19: Map of the baselines that have significant length extension

5.3 Long term strain rates

5.3.1 Network strain rates

Using both the CSI and SAGENZ networks, a comparison of the long term strain rates can be made. This compares the CSI campaign data spanning 8 years (1994-2002) with the SAGENZ CGPS data from the permanent sites spanning 4.78 years (February 2000 – October 2004).

To determine strain (or strain rates), stations from each network are triangulated using Delaunay triangulation. This results in a network connecting stations through optimally chosen equilateral triangles. Doing this for both the CSI and SAGENZ networks would result in triangles with sides of between 5-20km. But comparing the strain rates of the two networks would be difficult as the network points do not, in general, coincide.

Instead, two triangles with sites that are within reasonable proximity of each other and therefore represent similar regions have been used. The SAGENZ sites used involve five CGPS sites, namely QUAR, KARA, CNCL, NETT and HORN. Listed in Table 12 are the

SAGENZ	CSI	Distance (m)
QUAR	6718 (JI Karangarua SD)	1.95km
KARA	6720 (JM Karangarua)	400m
CNCL	6732 (Conical Hill)	2m
NETT	6700 (M Mt Hodgkinson)	4.3km
HORN	6700 (M Mt Hodgkinson)	1.2km

Table 12: CSI and SAGENZ sub-network points

sites used in both networks and the approximate distance between the campaign sites (CSI) and the CGPS sites (SAGENZ). Although NETT is a CGPS site, the data quality is not as good as the other sites. There are several long data outages and although the bad data and seasonal trends have been removed, there could still be a bias in the estimated site velocity. A second estimate of the strain can be determined using the CGPS site HORN, which is located at a lower elevation down in the Tasman valley. There is less data from this site (just under two years), but the data is of higher quality and almost continuous.

To compare the measured strain rates, three sub-networks that include sites from both the CSI and SAGENZ networks are considered. Sub-network 1 is a small triangle with sides between 9-16km, straddling the Alpine fault. Sub-network 2 covers a larger region from the Alpine fault to just east of the main divide, a distance of over 30km. Sub-network 3 computes an average strain rate using both the semi-CGPS and CGPS SAGENZ sites (excluding MTJO) and a selection of the CSI sites. The estimated engineering strain rates $(\dot{\gamma}_1, \dot{\gamma}_2)$, maximum shear strain rate $(\dot{\Gamma})$ and eigenvalue strain rates $(\dot{\varepsilon}_1, \dot{\varepsilon}_2)$ are given in Table 13. The eigenvalue strain rates for each sub-network are given in Figure 20 and Figure 21.

Sub-network 1: This sub-network involves the CSI sites 6718, 6720, 6732 (Figure 20) and the SAGENZ sites QUAR, KARA, CNCL (Figure 21 and also Table 13). The extension strain rate for both networks is similar (0.24±0.01ppm/yr), but the contraction strain rate for the SAGENZ (-0.33±0.01ppm/yr) is twice that of the CSI network. The orientation of the principal axis of contraction of both networks agrees within the statistical uncertainty. The estimated precision, from the CGPS data (SAGENZ network), is improved by approximately an order of magnitude, (spans 4.78 years compared to a span of 8 years for the campaign

Engineering Shear Strain Rates $\dot{\gamma}_1$ $\mu rad/yr$	$\dot{\gamma}_2$ $\mu rad/yr$	Maximum Shear Strain Rate $\dot{\Gamma}_2$ $\mu rad/yr$	Eigenvalue Strain Rates $\dot{\varepsilon}_1$ ppm/yr	$\dot{\varepsilon}_2$ ppm/yr	Maximum Direction of Contraction θ°	Network	Time Span *years*	Triangle
Sub-network 1								
-0.363±0.162	0.200±0.174	0.415±0.168	0.249±0.094	-0.166±0.135	104.4±12.0	CSI	8	6718, 6720, 6732
-0.532±0.013	0.203±0.013	0.569±0.016	0.240±0.012	-0.330±0.008	100.5±1.2	SAGENZ	4.7	QUAR, KARA, CNCL
Sub-network 2								
-0.300±0.113	0.406±0.119	0.505±0.123	0.369±0.106	-0.136±0.054	116.8±6.9	CSI	8	6718-6732-6700
-0.208±0.016	0.599±0.020	0.634±0.021	0.501±0.017	-0.133±0.009	125.4±0.8	SAGENZ	4.7	QUAR, CNCL, NETT
-0.254±0.015	0.453±0.018	0.519±0.020	0.392±0.016	-0.126±0.008	120.4±1.0	SAGENZ	4.7	QUAR, CNCL, HORN
Sub-network 3								
0.674±0.116	0.571±0.161	0.883±0.11	0.39±0.090	-0.50±0.061	110.1	CSI (Beavan *et al.*, 1999)	4	6702, 6715, 6718, 6719, 6720, 6732, 6733, 6735, 6736, 6706, 6737, 6714, 6734
-0.271±0.025	0.253±0.025	0.371±0.026	0.219±0.022	-0.151±0.012	111.6±2.0	CSI	8	6702, 6715, 6718, 6719, 6720, 6732, 6733, 6735, 6736, 6706, 6737, 6714, 6734
-0.416±0.008	0.423±008	0.593±010	0.345±0.008	-0.249±0.004	112.7±0.5	SAGENZ	4.7	QUAR, CNCL, KARA, NETT, HORN, PILK, REDD, MAKA, LEOC, VEXA

Table 13: Engineering shear and eigenvalue strain rates for the CSI and SAGENZ. The engineering shear parameter, $\dot{\gamma}_1$, measures the increase in the right angle between rays pointing NW and NE; $\dot{\gamma}_2$ measures the decrease in a right angle between a ray pointed north and one pointed east. The eigenvalue strain parameters, $\dot{\varepsilon}_1$ and $\dot{\varepsilon}_2$ are in the directions of the principal axes (eigenvectors). By convention, extension is positive, $\dot{\varepsilon}_1 > \dot{\varepsilon}_2$, and θ is measured clockwise from north to the principal axis of the contraction eigenvalue.

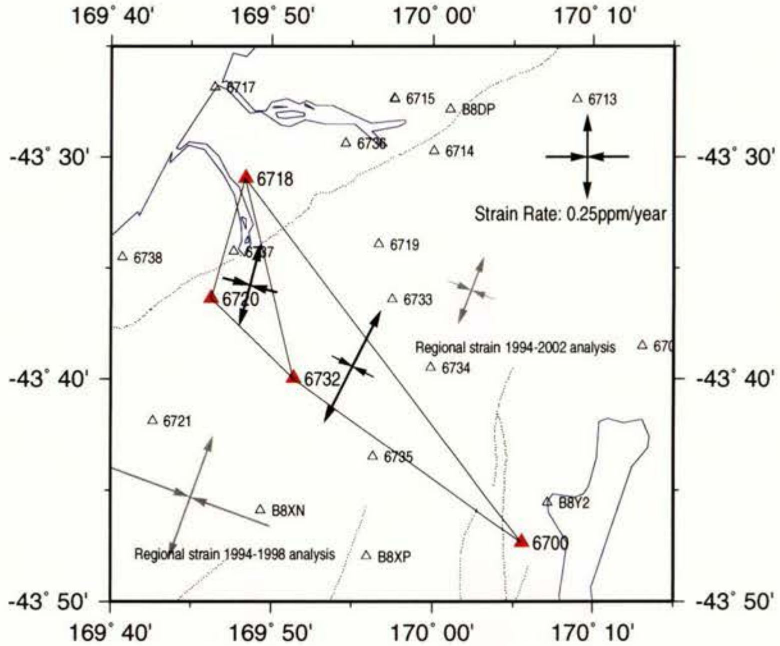

Figure 20: Principal axes of the horizontal eigenvalue strain rate for the CSI sub-networks. For each triangle, contraction is represented by the inward pointing arrows, extension by the outward pointing arrows. The strain figure outside the sub-network (grey) represents the strain rate in the region computed from 13 sites (6702, 6715, 6718, 6719, 6720, 6732, 6733, 6735, 6736, 6706, 6737, 6714, 6734) and depicted in Figure 6 of Beavan *et al.* (1999)

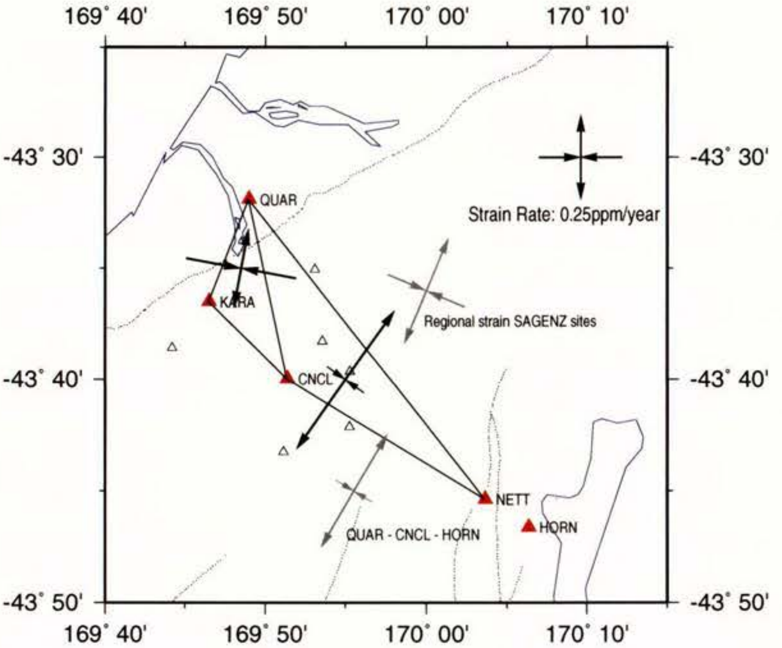

Figure 21: Principal axes of the horizontal eigenvalue strain rate for the SAGENZ sub-networks. For each triangle, contraction is represented by the inward pointing arrows, extension by the outward pointing arrows. The two strain figures outside the sub-networks (grey) represent the strain rate computed from 11 SAGENZ sites (QUAR, WAKA, CNCL, KARA, NETT, HORN, PILK, REDD, MAKA, LEOC, VEXA) (upper strain figure) and the strain rate computed from the triangle (QUAR, CNCL, HORN) (lower strain figure).

data). This improvement in precision is, for the most part, due to using permanent (non-changing) equipment on solid monuments but also, to a lesser degree, due to overall satellite configuration and receiver/antenna technology improvements.

Sub-network 2: This sub-network involves the CSI sites 6718, 6732, 6700 (Figure 20) and the SAGENZ sites QUAR, CNCL, NETT (Figure 21 and also Table 13). The extension and contraction strain rates and the principal axis of contraction determined from the CSI and SAGENZ networks agree within the statistical uncertainties. The contraction rates are practically identical, but the SAGENZ extension rate is greater by approximately 1/3 compared to the CSI network causing a significant change in the areal dilatation.

Given the poor data quality at the NETT site, strain rate estimates have also been computed using the HORN site. Even though the data covers a shorter period of time (~2 years), the horizontal component of the velocity should be well determined. The extensional strain rate decreases from 0.50±0.02ppm/yr to 0.39±0.02ppm/yr, which is closer to the 0.37±0.11ppm/yr estimated by the CSI network (Table 13, and the lower strain rate figure (grey) in Figure 21). The orientation and contraction strain rates do not change substantially. The contraction rates are not significantly different but the extension rate is (just) significantly different at the 1% significance level.

Sub-network 3: The final sub-network estimates an average strain rate over the respective regions. The CSI sub-network includes the five sites used in sub-networks 1 and 2 and the sites surrounding, but mainly to the immediate north, of the SAGENZ network (Figure 20). The estimated extension and contraction strain rates are 0.22±0.02 ppm/yr and -0.15±0.01 ppm/yr respectively and is depicted by the upper strain rate figure (grey) in Figure 20. When compared to the values given in Beavan *et al.* (1999), both strain rate values based on the CSI data spanning 8 years decrease (Table 13 and the lower strain rate figure (grey) in Figure 20). The contraction strain rate is statistically different (at the 1% significance level).

A comparison with the SAGENZ data based on the 11 SAGENZ sites, including both CGPS and semi-CGPS sites (but excludes MTJO), can also be made. The estimated extension and contraction strain rates are 0.35±0.008 ppm/yr and -0.25±0.004 ppm/yr respectively and is depicted by the upper strain rate figure (grey) in Figure 21. Compared to the CSI network spanning 8 years, this is an increase in both the extension and contraction strain rates of approximately 60%. The extension rates do not agree within the statistical uncertainty. But care must be taken with any comparison as the CSI and SAGENZ regions over which the strain is estimated are not identical. The orientations of the maximum contraction do not change substantially.

For sub networks 1 and 2, both the CSI and SAGENZ estimates of the extension and contraction strain rates agree within the statistical uncertainty of the measurements at the 1% significance level. Sub-network 1 that straddles the Alpine fault and sub-network 2 covers the region between the Alpine fault and just east of the main divide. There is less agreement, when averaging the strain rate for multiple, but not identical, sites from the Alpine fault to east of the Main Divide (sub network 3), where both the extension and contraction strain rates increase.

5.3.2 Network areal dilation

The areal dilation for each network, given in Table 14, is the sum of the two eigenvalue strain rates, namely $\dot{\varepsilon}_1 + \dot{\varepsilon}_2$. Except for the SAGENZ sub-network 1 (QUAR-KARA-CNCL) and the CSI sub-network 3, all the areal dilation estimates are positive. This indicates that there is an extensional regime with $|\dot{\varepsilon}_1| > |\dot{\varepsilon}_2|$ i.e. $\dot{\varepsilon}_1 + \dot{\varepsilon}_2 > 0$, and hence increase in area (area creation). Since the Southern Alps are caused by convergence across the plate boundary zone and as the Alpine Fault is an oblique thrust fault, it could be expected that there is an overall contraction. However, elastic dislocation theory does predict a zone of extension above the hanging wall of a thrust fault during periods of strain accumulates between earthquakes. The

Eigenvalue Strain Rates		Areal Dilation	Maximum Direction of Contraction	Network	Time Span	Triangle
$\dot{\varepsilon}_1$ ppm/yr	$\dot{\varepsilon}_2$ ppm/yr	$\dot{\varepsilon}_1 + \dot{\varepsilon}_2$ ppm/yr	θ°		$years$	
Sub-network 1						
0.249±0.094	-0.166±0.135	0.083±0.164	104.4±12.0	CSI	8	6718, 6720, 6732
0.240±0.012	-0.330±0.008	-0.090±0.014	100.5±1.2	SAGENZ	4.7	QUAR, KARA, CNCL
Sub-network 2						
0.369±0.106	-0.136±0.054	0.233±0.118	116.8±6.9	CSI	8	6718-6732-6700
0.501±0.017	-0.133±0.009	0.368±0.019	125.4±0.8	SAGENZ	4.7	QUAR, CNCL, NETT
0.392±0.016	-0.126±0.008	0.266±0.018	120.4±1.0	SAGENZ	4.7	QUAR, CNCL, HORN
Sub-network 3						
0.39±0.09	-0.50±0.061	-0.11±0.108	110.1	CSI (Beavan *et al.*, 1999)	4	6702, 6715, 6718, 6719, 6720, 6732, 6733, 6735, 6736, 6706, 6737, 6714, 6734
0.219±0.022	-0.151±0.012	0.068±0.025	111.6±2.0	CSI	8	6702, 6715, 6718, 6719, 6720, 6732, 6733, 6735, 6736, 6706, 6737, 6714, 6734
0.345±0.008	-0.249±0.004	0.096±0.009	112.7±0.5	SAGENZ	4.7	QUAR, CNCL, KARA, NETT, HORN, PILK, REDD, MAKA, LEOC, VEXA

Table 14: Eigenvalue strain rates and areal dilation for the CSI and SAGENZ. Conventions given in Table 13.

noticeable difference is that although the areal dilation determined by the CSI data indicates extension, the errors are considerably larger and the dilation is only marginally significant. In contrast, the precision of the areal dilation determined from the SAGENZ data is considerably better, thereby providing a result that is better determined.

This is an interesting result since the Alpine fault is predominantly strike-slip with a significant contribution of reverse slip with sub-networks 2 and 3 extend across the most tectonically active part of the central Southern Alps. It is worth noting that (Walcott 1998, see Figure 22) documented the existence of normal faults east of the Alpine Fault.

5.3.3 SAGENZ Sub-network strain rates

The eigenvalue strain rates, engineering strain rates and areal dilation rates using all the semi-CGPS and CGPS sites are given in Table 15. For the 10 sites (excluding HORN), Delaunay triangulation derives a network of 13 triangles. The strain rates for three additional triangles are also determined by replacing NETT with HORN. This corresponds to the three eastern most triangles. The eigenvalue strain rates are plotted in (Figure 22). Subdividing the whole network into smaller triangles provides much more detail on how the strain rates vary in the region.

Two of the triangles that include LEOC (western most site) show significantly high strain rates. For the western most triangle, the high contraction rate is most probably due to the north-south elongated triangle. The triangle does not have a significant east-west spatial extent and therefore the contraction strain rate is poorly determined. The anomalous strain rate could also be due to an inconsistent velocity at LEOC compared to the overall SAGENZ profile or that the region is in some way deforming differently (see also Section 5.1).

One pattern that emerges is an overall increase in the contraction strain rate from east to west. The triangles with the smallest contraction rates are generally those associated with NETT (or HORN), while those triangles closest to the Alpine fault have the largest contraction strain rates (but excluding the triangle QUAR-KARA-LEOC). The precision estimates of the strain rate parameters are generally at least twice those of the three sub-networks discussed in Section 5.3.1.

There is also evidence for along strike variation in the geodetic strain rate. Current tectonic models of the central Southern Alps assume the Alpine fault trends at 55° with possibly a second parallel antithetic structure at the same strike, but opposite dip, located some hundred kilometres to the SE. The expected gradient of the strain rate is along a line perpendicular to both structures (i.e., in the SE-NW direction), while position along the plate boundary zone (NE-SW direction) should not affect the strain rate (significantly). However, the three triangles that include NETT (or HORN) have significantly different strain rates even though each region is about the same distance from the Alpine fault with the northern side of the profile having a greater extension than the southern side (see also Figure 22). This pattern of greater extension to the north of the profile is also seen in the triangle WAKA-VEXA-REDD, even though it is closer to the Alpine fault. It suggests that there is a localised area undergoing extension in the region of the network bounded by WAKA, PILK, VEXA and NETT (or HORN).

A shear strain pattern without any significant dilatation or areal contraction is typical near an oblique reverse predominantly strike-slip fault such as the Alpine fault. Although much of the network does not have significant areal dilation (contraction or extension) there are regions with both significant areal contraction and areal extension (Figure 23). Comparing the strain rates for the northern regions with triangles at comparable distances from the fault on the southern side of the transect, suggests a pattern of extension along a NW-SE axis dominates along the northern side of the transect.

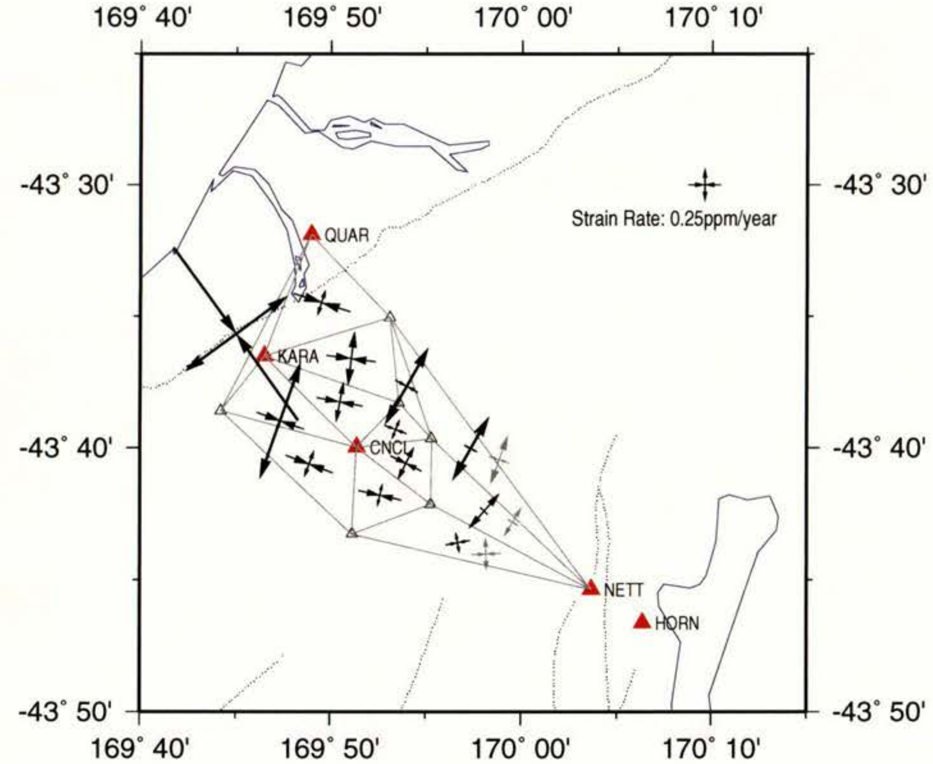

Figure 22: Principal axes of the horizontal eigenvalue strain rate for all the SAGENZ sub-networks. For each triangle, contraction is represented by the inward pointing arrows, extension by the outward pointing arrows. For the three eastern most triangles that are connected to NETT, the strain rate using HORN instead of NETT are shown in grey. Note the smaller strain rate scale than in Figure 20 and Figure 21.

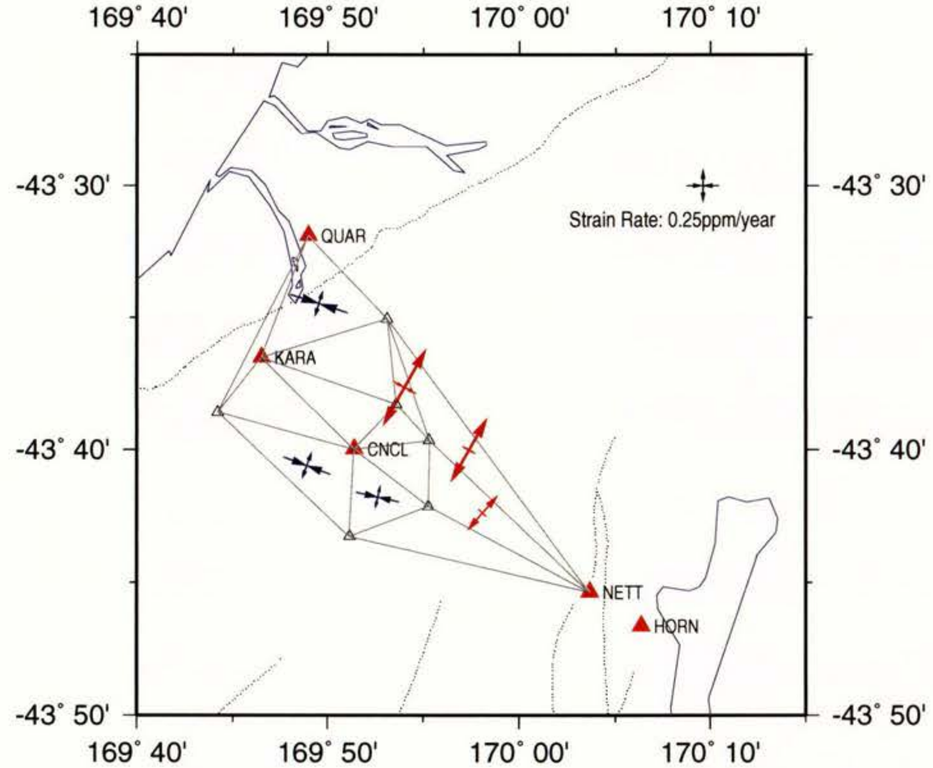

Figure 23: Principal axes of the horizontal eigenvalue strain rates for triangles where the areal dilation is significant (1% significance level). Strain rates with significant contraction shown in blue $(\dot{\varepsilon}_1 + \dot{\varepsilon}_2 < 0)$, strain rates with significant extension shown in red $(\dot{\varepsilon}_1 + \dot{\varepsilon}_2 > 0)$.

Engineering Shear Strain Rates		Maximum Shear Strain Rate	Eigenvalue Strain Rates		Areal Dilation	Maximum Direction of Contraction	Triangle
$\dot{\gamma}_1$ $\mu rad\ /\ yr$	$\dot{\gamma}_2$ $\mu rad\ /\ yr$	$\dot{\Gamma}$ $\mu rad\ /\ yr$	$\dot{\varepsilon}_1$ $ppm\ /\ yr$	$\dot{\varepsilon}_2$ $ppm\ /\ yr$	$\dot{\varepsilon}_1 + \dot{\varepsilon}_2$ $ppm\ /\ yr$	θ°	
-0.539±0.018	0.374±0.019	0.657±0.017	0.207±0.012	-0.450±0.013	**-0.243±0.018**	107.4±0.8	QUAR, KARA, WAKA
0.771±0.104	2.420±0.125	2.540±0.129	0.949±0.055	-1.590±0.104	**-0.641±0.118**	-36.2±1.3	QUAR, KARA, LEOC
-0.754±0.029	0.185±0.024	0.776±0.029	0.408±0.028	-0.368±0.009	0.040±0.029	96.9±0.9	KARA, WAKA, VEXA
-0.605±0.032	0.234±0.030	0.649±0.034	0.301±0.030	-0.348±0.015	-0.047±0.033	100.6±1.4	KARA, VEXA, CNCL
-1.010±0.033	0.819±0.032	1.300±0.036	0.923±0.032	-0.380±0.012	**0.543±0.034**	109.5±0.8	KARA, CNCL, LEOC
-0.439±0.091	0.734±0.113	0.855±0.114	0.659±0.079	-0.195±0.065	**0.464±0.102**	119.6±3.5	VEXA, WAKA, PILK
-0.249±0.056	0.225±0.048	0.336±0.050	0.157±0.043	-0.178±0.031	-0.021±0.053	111.1±4.2	VEXA, PILK, CNCL
-0.448±0.038	0.387±0.033	0.592±0.038	0.214±0.035	-0.378±0.013	**-0.164±0.038**	110.4±1.8	CNCL, MAKA, LEOC
-0.326±0.043	0.424±0.038	0.534±0.042	0.271±0.039	-0.263±0.018	0.008±0.043	116.2±2.3	PILK, CNCL, REDD
-0.454±0.043	0.219±0.043	0.504±0.046	0.174±0.037	-0.330±0.024	**-0.156±0.044**	102.8±2.6	CNCL, REDD, MAKA
-0.334±0.044	0.571±0.047	0.661±0.051	0.554±0.045	-0.107±0.017	**0.447±0.048**	119.8±2.2	PILK, WAKA, NETT
-0.058±0.046	0.415±0.043	0.419±0.045	0.347±0.044	-0.072±0.008	**0.275±0.045**	131.0±3.2	PILK, REDD, NETT
-0.328±0.060	-0.127±0.049	0.352±0.056	0.164±0.052	-0.188±0.025	-0.024±0.057	79.5±3.8	REDD, MAKA, NETT
Additional three triangles replacing NETT with HORN							
-0.432±0.049	0.356±0.054	0.560±0.056	0.399±0.045	-0.161±0.029	**0.238±0.053**	109.8±2.9	PILK, WAKA, HORN
-0.169±0.049	0.318±0.048	0.360±0.052	0.263±0.047	-0.098±0.018	**0.165±0.050**	121.0±4.2	PILK, REDD, HORN
-0.484±0.062	-0.030±0.051	0.485±0.061	0.258±0.058	-0.227±0.021	0.031±0.061	88.2±3.0	REDD, MAKA, HORN

Table 15: Engineering shear, eigenvalue strain and areal dilation strain rates for the SAGENZ network. Triangles with significant areal dilation are bolded (1% significance level). The triangle QUAR, KARA, LEOC is thought to be anonmoulous. Conventions given in Table 13.

6 Temporal Strain Variation

It is clear that most of the sites in the SAGENZ network are subject to seasonal signals as a result of the climatic effects in the region. In particular, we may be observing the elastic response of a surface load, probably due to seasonal ice/snow loading along the Southern Alps, which causes localised horizontal and vertical displacements of the GPS sites. The effect of pore fluids may also be important with "spongy" rock beneath sites swelling as snowmelt fills up cracks during spring to summer; followed by shrinking as the rock drains (Hager 2004). The actual observed site displacement at each site will be affected by the quantity of snow and ice accumulated during the winter months and subsequent spring melt, which in turn is a function of a site's elevation (e.g. topography around higher sites will collect more snow and ice), and the distance from the main divide. The orientation of the topography on a surface load will also influence the displacement, for example, a ridge that runs parallel to the main divide will be displaced in a different manner to a ridge that is perpendicular to the main divide. It is also possible that some of the observed cyclical pattern could be attributed to changing multipath characteristics of each site.

Ideally, we would like to be able to determine the strain of a particular region on a day by day basis and therefore be able to monitor a change in the strain pattern over time. The precision of the long term strain rates given in Section 5.3 is, in part, due to the long time period over which the data is collected (i.e. 8 years for the CSI network and 4.7 years for SAGENZ network). To determine the change in strain over a shorter period of time requires the computation of velocities over shorter time periods and hence a decrease in the precision of the deformation parameters.

In this section, the strain parameters have been derived from the day to day coordinate displacements after removal of the secular velocity. The strain parameter estimates are therefore an averaging of the site displacements. The day to day noise in the station coordinates (horizontal component) is in the order ±1-3mm rms, which in turn is seen as noise in the strain parameter estimates. Although there will be some averaging of the noise, what should be visible is any systematic coordinate displacement for a group of stations that manifests as a change in strain. We therefore expect to see structure in the strain parameters when there is consistent movement between several sites.

To demonstrate this we initially use a triangle that has significant seasonal displacements (QUAR-CNCL-PILK). We then remove the seasonal displacements from each station and analyse the estimated strain variation.

6.1 Temporal strain variation – with seasonal displacements

6.1.1 QUAR-CNCL-PILK

The best example in the SAGENZ network is the triangle QUAR-CNCL-PILK. The seasonal displacements at both QUAR and CNCL are reasonably small with amplitudes at the 1mm level, while the horizontal displacement at PILK is in the order of 7mm. Figure 24 graphs the strain extension and contraction plotted both as a continuous time series (years) and also when all years are stacked together (i.e. strain variation plotted per day of year (DOY)). As expected, it is clear that the (surface) strain caused by the site displacements results in a cyclical strain variation. Minimum extension is observed during the first half of each year and maximum extension during the second half. The peaks occur during March (minimum ~DOY 50) and October (maximum ~DOY 290).

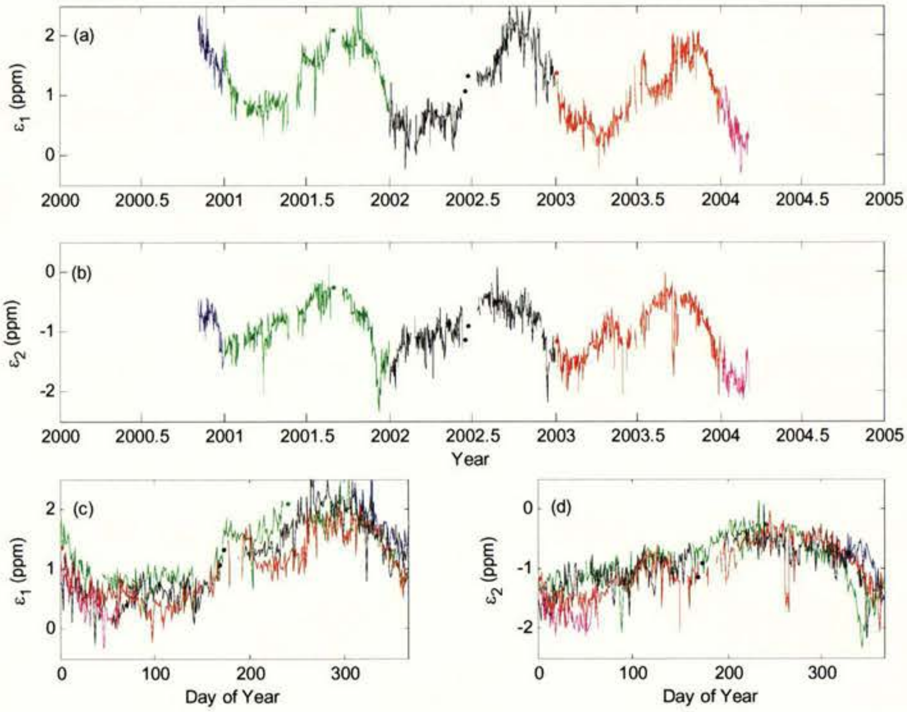

Figure 24: Temporal strain variation. Graphs (a) and (b) plot extension (ε_1) and contraction (ε_2) over time in years. Graphs (c) and (d) plot extension and contraction over time in day of year (DOY). Line colours represent 2000 (blue), 2001 (green), 2002 (black), 2003 (red) and 2004 (magenta).

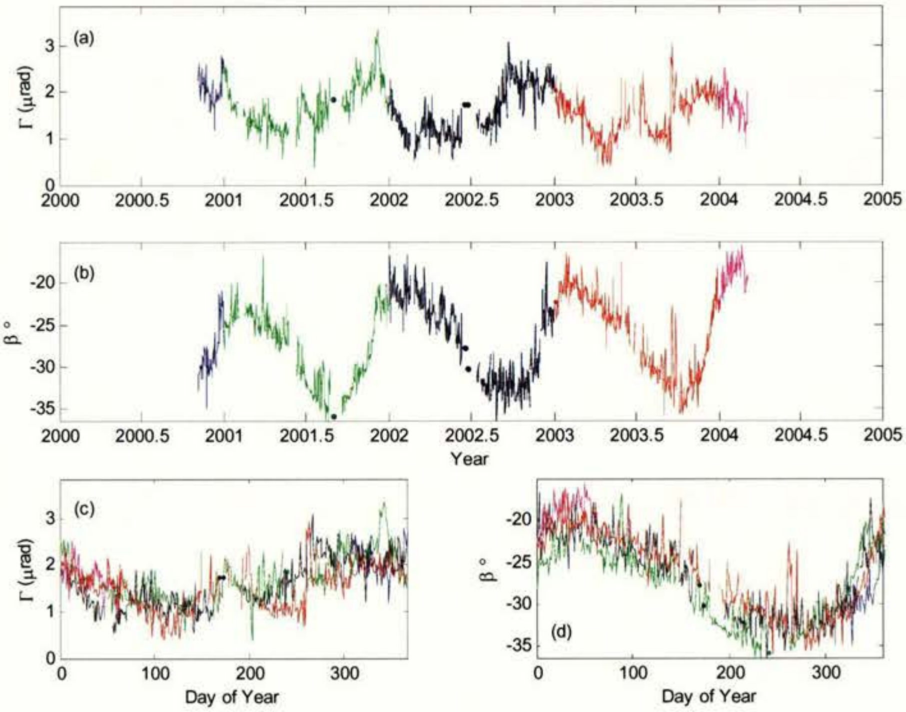

Figure 25: Graphs (a) and (b) plot the maximum shear strain (Γ) and second graph plots orienation of maximum shear strain (β^o) over time in years. Graphs (c) and (d) plot maximum shear strain and orienation per day of year (DOY). Line colour representation as per Figure 24.

The compressive component behaves differently compared to the extensional component. There is a more constant decrease in contraction (-1.5ppm to -0.5ppm) from the beginning of the year through to August (DOY 225), followed by a rapid increase in contraction until the end of the year. This corresponds to the period from spring to early summer where the environment experiences an increase in the daily temperature, increased melt water through the thawing of ice and snow, and a corresponding decrease in the volume of snow and ice.

A similar (but not identical) pattern is seen when the maximum shear strain (Γ) and the orientation of the maximum shear strain (β^o) are plotted (Figure 25). The direction of the maximum shear strain varies very regularly between -20° in February to -35° in September.

Although there is a high noise level, similar systematic patterns are seen at most other sites to some degree. The QUAR-KARA-PILK sub-network is particularly good due to having nearly three years of data with only small data outages and the large horizontal site displacement at PILK. This strain variation **cannot** be interpreted as a regional change in strain; rather it represents a localised strain variation caused by localised (surface) station displacements. It does, however, provide a mechanism for monitoring, on a day to day basis, changes in a particular set of stations (in this case three sites). Any systematic site motion that occurs at all sites that is over and above the seasonally induced (localised) site displacements should be detected as an abnormal strain variation.

6.2 Temporal strain variation – corrected for seasonal displacements

6.2.1 Sub network QUAR-CNCL-PILK

The strain variation depicted by the sites QUAR-CNCL-PILK is seasonally induced. Correcting for the seasonal displacements will remove most of the systematic variations seen in Figure 24 and Figure 25. The corrected strain and maximum shear components are show in Figure 26 and Figure 27 respectively.

Certainly the range of the strain is reduced from 2ppm to 0.5ppm in both the extension and contraction strain components (Figure 26). It is most likely that most of the variation in the strain parameters is caused by positional errors (noise). This results in an average error of the eigenvalue strain parameters ranging from ±0.44ppm to ±0.53ppm. For clarity, the graphs that follow have not been plotted with the strain parameter errors.

There does appear to be some structure in the extensional strain when plotted per day of year (Figure 26c). There is a period of relatively less variation or more consistent strain extension for the three months from May until August (approximately DOY 125 to DOY 225), which corresponds with late autumn till early winter. After this period (between October-November) the extension strain variability increases corresponding to the period when there is increasing daily temperatures, increasing snow and ice melt and a decrease in snow and ice loading. The strain contraction component has increased variability that is greatest during the end/start of each year compared to the extensional strain component. There is not a clearly defined period when there is less variation.

Both the strain extension and contraction still appear to have small cyclical trends that are correlated. The plot of the areal dilatation (Figure 27a, c) describes the overall change in (horizontal) area, with a peak to peak range in the order of 2ppm. The dilatation is a maximum (increase in area) during April (DOY 90-120) and November (DOY 305-335), and

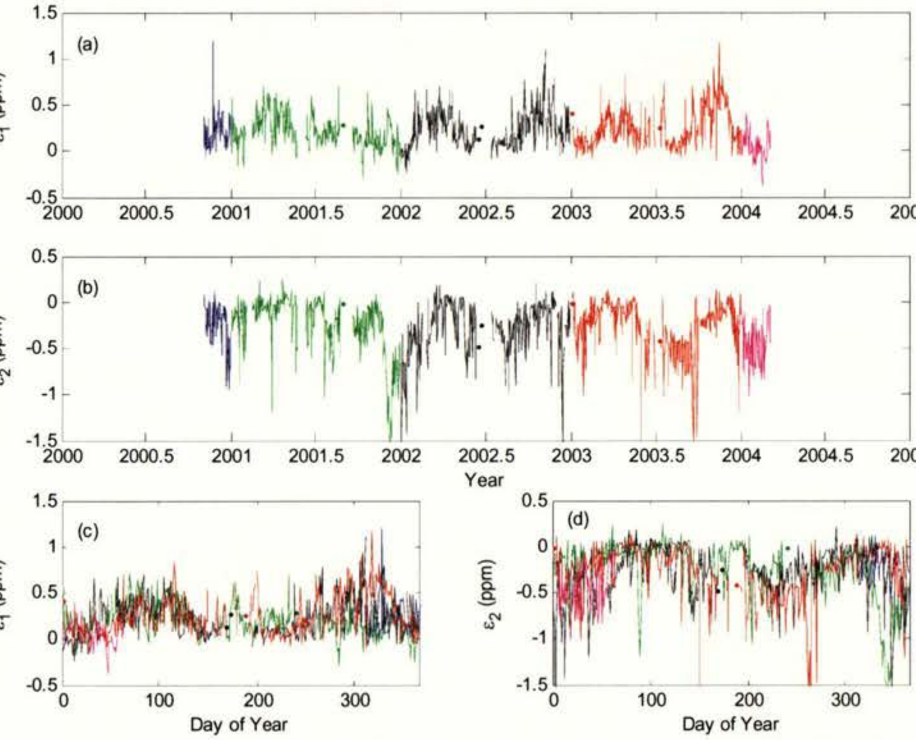

Figure 26: Temporal strain variation corrected for seasonal displacements. Graph (a) plots extension (ε_1) and graph (b) contraction (ε_2) over time in years. Graphs (c) and (d) plot extension and contraction per day of year (DOY). Line colour representation as per Figure 24.

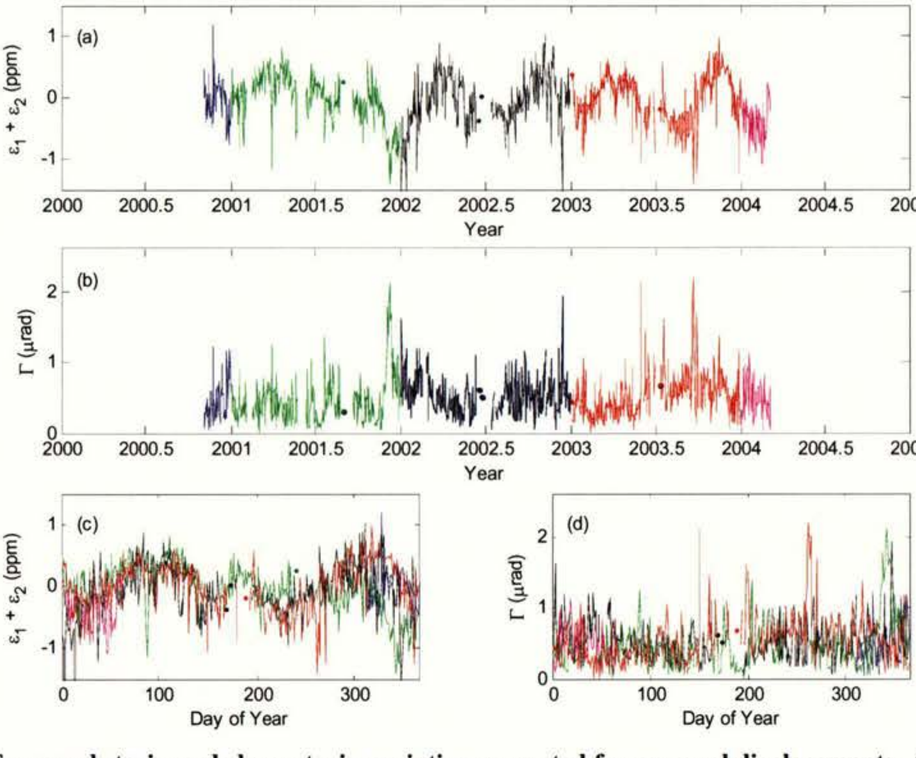

Figure 27: Temporal strain and shear strain variation corrected for seasonal displacements. Graph (a) plots the areal dilatation (ε_1+ε_2) and graph (b) maximum shear strain (Γ) over time in years. Graphs (c) and (d) plot areal dilatation and maximum shear strain per day of year (DOY). Line colour representation as per Figure 24.

a minimum (area contraction) during both the middle of the year (June-August) and the end/start of each year (December-January). Although the trend is well defined, it is also noisy and care must be taken with any interpretation.

The apparent change in dilation may also be an artefact of our ability to model the seasonal site displacements, which have been corrected using the estimated annual or annual plus semi-annual terms. There may also be residual site motion that is not adequately modelled. This is seen in the case of PILK (Section 4.3.4, Figure 14), where the annual and semi-annual terms adequately model the east component during most of 2002 and 2003, but there is a noticeable departure during the spring of 2001 and early summer of 2002. During this period, the mark actually moves both further west and starts to move in a westerly direction earlier than predicted by the model. A second noticeable difference is at the start of 2004 where the mark again moves further west by about 5mm than the model predicts. A smaller deviation between the actual observed and predicted motion can be observed for the north component.

Similar observations can be made for other sites. For example, both KARA and CNCL have cyclical site movements that tend to be more erratic than other sites such as QUAR. They are all likely to be environmentally induced, but differ due to different local conditions. All such un-modelled displacements contribute to the strain parameter estimates and will, in general, give rise to the overall noise level seen.

The cyclical patterns that are evident in the strain components are not so discernable in the maximum shear (Figure 27b, d), which is consistently noisy throughout the year at the 1ppm level.

6.2.2 Sub network QUAR-KARA-CNCL

This sub-network has the advantage of including the three CGPS sites with the longest data records. It therefore provides the best, year by year, indication of the degree of strain variation from the sites in the SAGENZ network. The sub-network also covers the region straddling the Alpine fault.

Much of the variation will be noise caused by the positioning errors, but some trends are apparent especially when each year is stacked. From year to year the temporal strain variation is different but there is consistently less variation in the extensional strain for about a month each year between DOY 175 and 200 (July). This seems to correspond to a positive gradient in the areal dilation (Figure 29c) indicating that the contractional strain component is decreasing at the same time as an increase in the extensional strain component.

Strain variations that are greater than normal can also be seen. During November and December 2002 there appeared to be an unusually large increase in the compressive strain (Figure 28(b)), (but no corresponding change in the extensional strain). Although there are other spikes, the increase appears to be of a longer duration. This bulge corresponds to a time when the site KARA appeared to move consistently to the east by about 10mm while CNCL moved westward by a similar amount (see Section 4.3.3, Figure 12 and Figure 13)

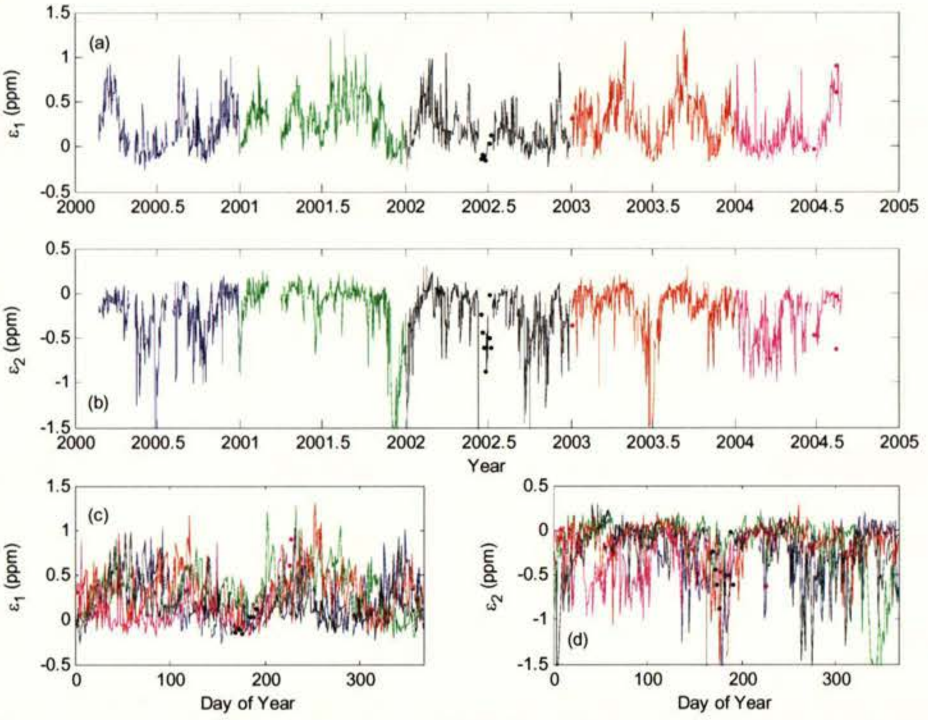

Figure 28: Temporal strain variation corrected for seasonal displacements. Graph (a) plots extension (ε_1) and graph (b) contraction (ε_2) over time in years. Graphs (c) and (d) plot extension and contraction per day of year (DOY). Line colour representation as per Figure 24.

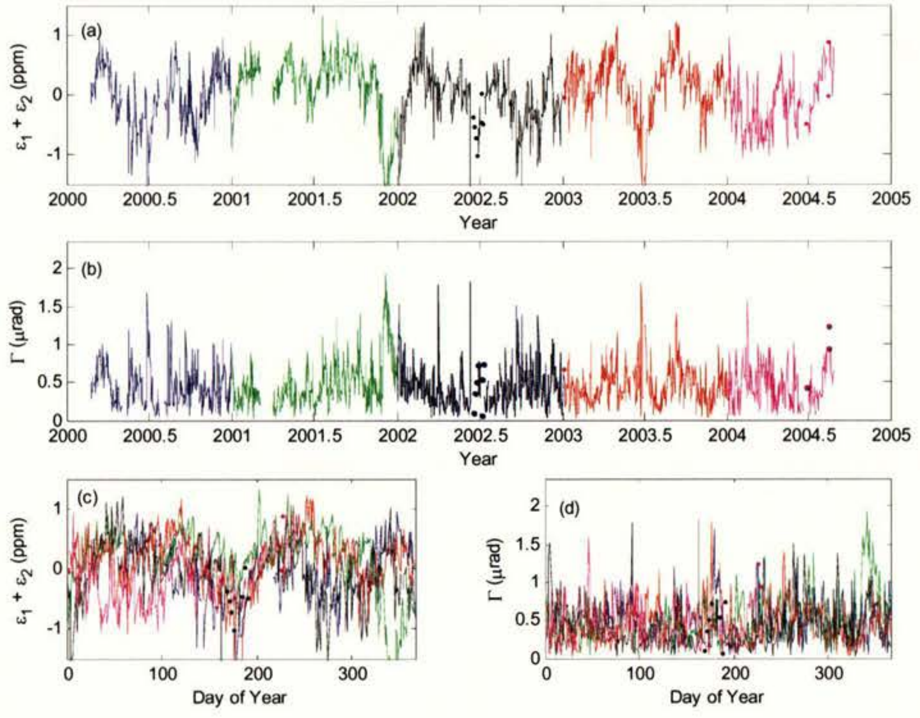

Figure 29: Temporal strain and shear strain variation corrected for seasonal displacements. Graph (a) plots the areal dilatation ($\varepsilon_1+\varepsilon_2$) and graph (b) maximum shear strain (Γ) over time in years. Graphs (c) and (d) plot areal dilatation and maximum shear strain per day of year (DOY). Line colour representation as per Figure 24.

7 Summary and Conclusions

This research project has investigated contemporary strain variation using the SAGENZ network of semi-CGPS and CGPS that crosses the Southern Alps between Karangarua to Mt Cook village. We have compared our strain rate estimates with those from a previous study and also investigated the temporal strain changes or strain variation in the same network. Previous geodetic work, typically using several GPS campaigns, has provided a picture of the geodetic strain spanning a period of years at the regional scale.

This project has contributed in the following ways:

- It has estimated velocities (and hence strain parameters) to a better level of precision than previously;
- It has demonstrated that there are significant localised seasonal site displacements;
- The strain rates derived from the site velocity estimates are broadly in agreement with previous work. However, there is evidence for strain variation through a region of high tectonic activity that has not been demonstrated in previous studies. This suggests that the tectonics of the Southern Alps are exceedingly complex;
- There appears to be seasonally induced systematic strain variations.

Network characteristics: The GPS data processing and network analysis resulted in a high quality time series of station positions. The daily horizontal coordinate repeatability is typically better than ±2mm rms and horizontal velocity estimates better than ±1mm/yr (1σ). The analysis had to take into account position offsets due to equipment changes (antenna changes) and also local seasonally induced site displacements.

One result that was not anticipated at the start of the project was the extent and magnitude of localised site displacements (see also Denys *et al.* 2003; Beavan *et al.* 2004). For the SAGENZ network stations, all sites exhibit some seasonally induced movement; several sites have some movement with amplitudes of up to 7-8mm, and one site (NETT) has an amplitude of at least 20mm.

The geophysical reasons for the site displacements are not fully understood at this stage. It is clear that the displacements are seasonally induced and that some sites are more erratic than others. The most likely reasons include snow and ice loading, rock porosity, thermoelastic strain as well as local effects such as topographic conditions and orientation. Most of the snow/ice loading will occur during autumn and winter followed by unloading during late spring and summer. As the Southern Alps rock is much fractured, rain and snow/ice melt will be absorbed into the rock through fractures. The rock porosity will affect the volume of groundwater contained in the rock. It is expected that groundwater will gradually drain from mountainous regions continuously through out the year and during periods when the surface is not frozen, it is likely that there is a net increase in groundwater causing the rock to swell. During periods when the surface is frozen there will be a gradual release of groundwater causing a net decrease in groundwater causing the rock to shrink.

Themoelastic strain is also likely to be induced by a combination of seasonal temperature changes and the angle of exposure of rock to heating effects from the sun. In such an environment it is likely that the displacements are a combination of processes. Irrespective of the actual cause, it has been demonstrated that mountainous regions are dynamic places that are subjected to the crustal deformation at the macro scale (plate tectonics) and micro scale (local environmental forces and topography), which in turn results in localised deformation effects. Although not investigated in this project, effects caused by changing multipath environments can not be discounted.

Network strain analysis: The velocity gradient across the network was determined and investigated in several ways. Using the SAGENZ data, the (Alpine) fault parallel and normal velocities were determined, and the strain parameters for several sub networks involving subsets of both the semi-CGPS and CGPS stations. In addition, the strain rates from the (localised) SAGENZ network were compared to those derived from the CSI regional campaign network that broadly covers the region between the East and West Coasts, Waitaki to Rakaia Rivers. Finally, a detailed investigation of the strain variability within the SAGENZ network is considered.

The fault parallel and normal velocities are similar to those given in (Beavan *et al.* 1999), although the precision obtained from the SAGENZ data is 50% better. Except for one site (LEOC) that appears to be inconsistent, the SAGENZ fault parallel velocities are slightly smaller.

Consistent with the velocity estimates, a comparison between the CSI and SAGENZ strain parameters shows that they are in general agreement (within the statistical uncertainties of the data), with the SAGENZ strain rate values being approximately an order of magnitude more precise. Using only the SAGENZ CGPS data, two sub networks involving 3 or 4 stations in each were compared with nearby sites from the CSI network. Although the CSI and SAGENZ strain rates and the orientation of the strain rates agree, with a denser network and the better precision of the SAGENZ data, there appears to be evidence of a zone of extension or increase in area.

A wider scale regional strain rate estimate using a subset of the CSI sites and all the SAGENZ sites was also made. Again the SAGENZ strain rates broadly agree with the CSI data, but there are differences that are statistically significant. In particular the SAGENZ contraction strain rate (-0.25±0.004 ppm/yr) is approximately double the rate determined from 8 years of CSI data. This is perhaps not surprising given that the sub networks being compared are not the same (the CSI sites cover a greater region), but does demonstrate that there is regional variability when investigating on a smaller scale.

Temporal strain variation: A second approach to looking at the variability of strain accumulation was to analysis the day to day change in strain relative to the secular velocity of each site. Only the CGPS sites (or sites with nearly continuous data records) were considered. To do this the seasonal signal was removed with a combination of annual and semi-annual terms. For each set of stations, the site displacements (after removal of the seasonal terms and site velocity) are used to compute the strain parameters.

For the two sub networks we considered (QUAR, CNCL, PILK and QUAR, KARA, CNCL), there is clearly structure to the strain parameter estimates (extension, contraction and areal dilation) that appears to correlated with the season (as observed above) and repeats on a year to year basis. There are periods during the year that clearly have greater variability (spring to early summer) when the daily temperature is increasing rapidly and greater snow/ice melting that results in less snow/ice loading. There are also periods with less variability that generally correspond to the winter periods when one would expect the underlying rock to be insulated with a covering of snow and ice.

We interpret this, for a particular station combination, to indicate that a region is extending or contracting on a small scale depending on how other processes (e.g. snow/ice loading, rock porosity, season temperature) are affecting it. This "localised" deformation is over and above the (regional) crustal deformation caused by the forces of plate tectonics. This observation also suggests that strain and/or velocity estimates from campaign GPS networks could have potentially significant positional errors owing to the measurements being carried out at different times in the annual cycle (as described above). As a result, the measurement of secular strain rates or velocities could be contaminated unless the measurement epochs happen to be made at the same time in the year so that the annual cycle cancels. (Note that in New Zealand, it is standard procedure to carry out repeat campaign measurements at the same time of year, thereby mitigating against such measurement biases.)

However, it must be emphasised that although there does appear to be structure to the temporal strain variation, the patterns that we see are very much at the noise level of the measurements. The average eigenvalue strain rate error is ±0.5ppm/yr when the range of eigenvalue strain is typically less than 1ppm/yr.

The major conclusion inferred from network strain analysis is an overall increase in the contraction strain rate from east to west. The triangles with the smallest contraction rates are generally those associated with NETT (or HORN), while those triangles closest to the Alpine fault have the largest strain contraction strain. A shear strain pattern without any significant dilatation or areal contraction is typical around an oblique reverse predominantly strike-slip fault such as the Alpine fault. Although much of the network does not have significant areal dilation (contraction or extension) there are regions with both significant areal contraction and areal extension. Comparing the strain rates for the northern regions with triangles at comparable distances from the fault on the southern side of the network suggests a pattern of extension along a NW-SE axis dominates along the northern side. The reason for this is still under investigation. Possible explanations are along strike variations of deformation style or subtle strain variations being caused by seasonally induced processes.

Some possible temporal strain variations can also be identified from a time series developed using the three CGPS sites with the longest data records after corrections for seasonal displacements have been applied. During November and December 2002 there appeared to be an unusually large increase in the compressive strain. Although there are other spikes, this increase appears to be of a longer duration. This anomaly is reflected in the velocity record and corresponds to a time when the site KARA appeared to move consistently to the east by about 10mm while CNCL moved westward by a similar amount. The cause of this anomaly has not yet been determined.

Acknowledgements

This research was funded by a grant from the Earthquake Commission (New Zealand) (EQC Project 01/457). Funding for the SAGENZ project was provided by Otago University (OU) (ORG MFWB03, ORG MFWB01), Foundation for Research, Science and Technology (FRST) (contracts C05X0203, C05X0402) and the National Science Foundation (NSF) (EAR9903183).

GPS data collection has been carried out by many field teams including the institutions involved in the SAGENZ project as well as the many different organisations involved in the collection of the CSI data. The Department of Conservation has been instrumental in granting of access and helicopter landing permits and there are several land owners who we have sort permission and access to their land.

We also thank Des Darby (GNS) and John Hannah (OU) for constructive reviews of this report.

Several figures were plotted using the public domain GMT software (Wessel and Smith 1995). Matlab Version 7.01 (R14) was used for data analysis and figures.

References

Anderson, H., T. Webb and J. Jackson (1993). *Focal Mechanisms of Large Earthquakes in the South-Island of New-Zealand - Implications for the Accommodation of Pacific-Australia Plate Motion*. Geophysical Journal International **115**(3): 1032-1054.

Beanland, S. (1995). *The North Island Dextral Fault Belt, Hikurangi Subduction Margin, New Zealand*. Unpublished PhD thesis. Victoria University of Wellington, Wellington, New Zealand

Beavan, J. and J. Haines (2001). *Contemporary Horizontal Velocity and Strain Rate Fields of the Pacific-Australian Plate Boundary Zone through New Zealand*. Journal of Geophysical Research Solid Earth **106**(B1): 741-770.

Beavan, J., D. Matheson, P. Denys, M. Denham, T. Herring, B. Hager and P. Molnar (2004). A Vertical Deformation Profile across the Southern Alps, New Zealand, from 3.5 Years of Continuous GPS Data. In T. v. Dam and O. Francis, (Eds) Proceedings of the workshop: The state of GPS vertical positioning precision: Separation of earth processes by space geodesy, Luxembourg, Cahiers du Centre Européen de Géodynamique et de Séismologie. **23:** 111-123.

Beavan, J., M. Moore, C. Pearson, M. Henderson, B. Parsons, S. Bourne, P. England, D. Walcott, G. Blick, D. Darby and K. Hodgkinson (1999). *Crustal Deformation During 1994-1998 Due to Oblique Continental Collision in the Central Southern Alps, New Zealand, and Implications for Seismic Potential of the Alpine Fault*. Journal of Geophysical Research-Solid Earth **104**(B11): 25233-25255.

Berryman, K. R., S. Beanland, A. F. Cooper, H. N. Cutten, R. J. Norris and P. R. Wood (1992). *The Alpine Fault, New Zealand: Variation in Quaternary Structural Style and Geomorphic Expression*. Annales Tectonicae **6**: 126-163.

Bibby, H. M. (1975). *Crustal Strain from Triangulation in Marlborough, New Zealand*. Tectonophysics **29**: 529-540.

Bibby, H. M. (1976). *Crustal Strain across the Marlborough Faults, New Zealand*. New Zealand Journal of Geology and Geophysics **19**: 407-425.

Bibby, H. M., A. J. Haines and R. I. Walcott (1986). *Geodetic Strain and the Present Day Plate Boundary Zone through New Zealand*. The Royal Society of New Zealand **Bulletin 24**: 427-438.

Bock, Y., S. Wdowinski, P. Fang, J. Zhang, S. Williams, H. Johnson, J. Behr, J. Genrich, J. Dean, M. Vandomselaar, D. Agnew, F. Wyatt, K. Stark, B. Oral, K. Hudnut, R. King, T. Herring, S. Dinardo, W. Young, D. Jackson and W. Gurtner (1997). *Southern California Permanent GPS Geodetic Array - Continuous Measurements of Regional Crustal Deformation between the 1992 Landers and 1994 Northridge Earthquakes*. Journal of Geophysical Research-Solid Earth **102**(B8): 18013-18033.

Bourne, S. J., T. Árdadóttir, J. Beavan, D. J. Darby, P. C. England, B. Parsons, R. I. Walcott and P. R. Wood (1998). *Crustal Deformation of the Marlborough Fault Zone in the South Island of New Zealand: Geodetic Constraints over the Interval 1982-1994*. Journal of Geophysical Research **103**(B12): 30147-30166.

Cowan, H. A. (1990). *Late Quaternary Displacements on the Hope Fault at Glynn Wey, North Canterbury*. New Zealand Journal of Geology and Geophysics **33**: 285-293.

Cowan, H. A. (1992). *Structure, Seismicity and Tectonics of the Porters Pass Fault Zone, North Canterbury, New Zealand*. Unpublished PhD thesis. University of Canterbury, Christchurch. New Zealand**:** 181pp

Cowan, H. A., A. Nichol and P. Tonkin (1996). *A Comparison of Historical and Paleoseismicity in a Newly Formed Fault Zone and a Mature Fault Zone, North Canterbury, New Zealand*. Journal Geophysical Research **101**: 6021-6036.

Davey, F. J. (1998). *Preliminary Results from a Geophysical Study across a Modern Continent-Continent Collision Plate Boundary - the Southern Alps of New Zealand*. Tectonophysics **288**: 221-235.

Davey, F. J. and E. G. C. Smith (1983). *The Tectonic Setting of the Fiordland Region, Southwest New-Zealand*. Geophysical Journal of the Royal Astronomical Society **72**(1): 23-38.

Denys, P., M. Denham, J. Beavan and D. Matheson (2003). Seasonal Crustal Motions Detected Using Continuous GPS. In Proceedings of the New Zealand Geophysical Society Annual Symposium, Victoria University of Wellington, Wellington.

Dong, D., P. Fang, Y. Bock, M. K. Cheng and S. Miyazaki (2002). *Anatomy of Apparent Seasonal Variations from GPS-Derived Site Position Time Series - Art. No. 2075*. Journal of Geophysical Research-Solid Earth **107**(B4): 2075-2075.

Dong, D., T. A. Herring and R. W. King (1998). *Estimating Regional Deformation from a Combination of Space and Terrestrial Geodetic Data*. Journal of Geodesy **72**(4): 200-214.

Eberhart-Phillips, D. and M. Reyners (2001). *A Complex, Young Subduction Zone Imaged by Three-Dimensional Seismic Velocity, Fiordland, New Zealand*. Geophysical Journal International **146**(3): 731-746.

Feigl, K. L., D. C. Agnew, Y. Bock, D. Dong, A. Donnellan, B. H. Hager, T. A. Herring, D. D. Jackson, T. H. Jordan, R. W. King, S. Larsen, K. M. Larson, M. H. Murray, Z. K. Shen and F. H. Webb (1993). *Space Geodetic Measurement of Crustal Deformation in Central and Southern California, 1984-1992*. Journal of Geophysical Research-Solid Earth **98**(B12): 21677-21712.

Feigl, K. L., R. W. King and T. H. Jordan (1990). *Geodetic Measurements of Tectonic Deformation in the Santa Maria Fold and Thrust Belt, California*. Journal of Geophysical Research **95**(B3): 2679-2699.

Hager, B. H. (2004). *Personal Communication*.

Hager, B. H., G. A. Lyzenga, A. Donnellan and D. Dong (1999). *Reconciling Rapid Strain Accumulation with Deep Seismogenic Fault Planes in the Ventura Basin, California*. Journal of Geophysical Research-Solid Earth **104**(B11): 25207-25219.

Hannah, J. (1984). *Accuracy Estimates of, and the Rejection Criteria Used on the Observed Quantities from the New Zealand Eds Networks*. The Royal Society of New Zealand **Bulletin 24**: 463-471.

Holt, W. E. and A. J. Haines (1995). *The Kinematics of the Northern South Island, New Zealand, Determined from Geologic Strain Rates*. Journal of Geophysical Research **100**: 17991-18010.

Hugentobler, U., S. Schaer and P. Fridez, Eds. (2001). Bernese GPS Software Version 4.2. Berne, Astronomical Institute, University of Berne.

Hull, A. G. and K. R. Berryman (1986). *Holocene Tectonism in the Region of the Alpine Fault at Lake McKerrow, Fiordland, New Zealand*. The Royal Society of New Zealand Bulletin **24**: 317-331.

Lebrun, J.-F., G. Lamarche and J.-Y. Collot (2003). *Subduction Initiation at a Strike-Slip Plate Boundary: The Cenozoic Pacific-Australian Plate Boundary, South of New Zealand*. Journal of Geophysical Research **108**(b9): 2435.

Leitner, B., B. D. Eberhart-Phillips, H. Anderson and J. L. Nabalek (2001). *A Focused Look at the Alpine Fault, New Zealand: Seismicity, Focal Mechanisms, and Stress Observations*. Journal of Geophysical Research **106**: 2193-2220.

Mangiarotti, S., A. Cazenave, L. Soudarin and J.-F. Crétaux (2001). *Annual Vertical Crustal Motions Predicted from Surface Mass Redistribution and Observed by Space Geodesy*. Journal of Geophysical Research **106**(B3): 4277-4291.

Mao, A. L., C. G. A. Harrison and T. H. Dixon (1999). *Noise in GPS Coordinate Time Series*. Journal of Geophysical Research-Solid Earth **104**(B2): 2797-2816.

McCalpin, J. P. (1996). *Tectonic Geomorphology and Holocene Paleoseismicity of the Molsworth Section of the Awatere Fault, South Island, New Zealand*. New Zealand Journal of Geology and Geophysics **39**(1): 33-50.

Norris, R. J. and A. F. Cooper (1995). *Origin of Small-Scale Segmentation and Transpressional Thrusting Along the Alpine Fault, New-Zealand*. Geological Society of America Bulletin **107**(2): 231-240.

Norris, R. J. and A. F. Cooper (2001). *Late Quaternary Slip Rates and Slip Partitioning on the Alpine Fault, New Zealand.* Journal of Structural Geology **23**(2-3): 507-520.

Norris, R. J., P. O. Koons and A. F. Cooper (1990). *The Obliquely-Convergent Plate Boundary in the South Island of New-Zealand - Implications for Ancient Collision Zones.* Journal of Structural Geology **12**(5-6): 715-725.

Pearson, C. (1991). *Distribution of Geodetic Strains across the Alpine Fault Zone near Haast, New Zealand.* Journal of Geophysical Research **96**(8465-8474).

Pearson, C. (1998). *Preliminary Geodetic Strain Measurements from the South Fiordland Region of New Zealand Using Repeat GPS Surveys - Implications for Subduction on the Puysegur Trench.* Geophysical Research Letters **25**(16): 3185-3188.

Pearson, C., P. Denys and K. Hodgkinson (2000). *Geodetic Constraints on the Kinematics of the Alpine Fault in the Southern South Island of New Zealand, Using Results from the Hawea-Haast GPS Transect.* Geophysical Research Letters **27**(9): 1319-1322.

Pearson, C. F. (1992). *Strain Measurements in the Northern Waiau Basin, South Island, New Zealand.* New Zealand Journal of Geology and Geophysics **35**: 375-379.

Pearson, C. F., J. Beavan, D. J. Darby, G. H. Blick and R. I. Walcott (1995). *Strain Distribution across the Australian-Pacific Plate Boundary in the Central South Island, New Zealand, from 1992 GPS and Earlier Terrestrial Observations.* Journal of Geophysical Research **100**(B11): 22071-22081.

Reilly, W. I. (1986). *Crustal Bending in Otago New Zealand, from the Evidence of Geodetic Measurements.* The Royal Society of New Zealand Bulletin **24**: 65-73.

Reyners, M. R., R. Robinson and P. McGinty (1997). *Plate Coupling in the Northern South Island and Southernmost North Island, New Zealand as Illuminated by Earthquake Focal Mechanisms.* Journal of Geophysical Research **102**: 15197-15210.

Shen, Z. K., M. Wang, Y. X. Li, D. D. Jackson, A. Yin, D. N. Dong and P. Fang (2001). *Crustal Deformation Along the Altyn Tagh Fault System, Western China, from GPS.* Journal of Geophysical Research-Solid Earth **106**(B12): 30607-30621.

Shen, Z. K., C. K. Zhao, A. Yin, Y. X. Li, D. D. Jackson, P. Fang and D. N. Dong (2000). *Contemporary Crustal Deformation in East Asia Constrained by Global Positioning System Measurements.* Journal of Geophysical Research-Solid Earth **105**(B3): 5721-5734.

Sibson, R. H., S. H. White and B. K. Atkinson (1979). *Fault Rock Distribution and Structure within the Alpine Fault Zone: A Preliminary Account.* The Royal Society of New Zealand **Bulletin 18**: 55-65.

Soudarin, L., J.-F. Crétaux and A. Cazenave (1999). *Vertical Crustal Motions from the Doris Space-Geodesy System.* Geophysical Research Letters **26**(9): 1207-1210.

Sutherland, R. and R. J. Norris (1995). *Late Quaternary Displacement Rate, Paleoseismicity and Geomorphic Evolution of the Alpine Fault: Evidence from Hokuri Creek, South Westland, New Zealand.* New Zealand Journal of Geology and Geophysics **38**(4): 419-430.

Tichelaar, B. W. and L. J. Ruff (1993). *Depth of Seismic Coupling Along Subduction Zones.* Journal of Geophysical Research **98**: 2017-2037.

van Dam, T. M., J. Wahr, P. C. D. Milly, A. B. Shmakin, G. Blewitt, D. Lavallée and K. M. Larson (2001). *Crustal Displacements Due to Continental Water Loading.* Geophysical Research Letters **28**(4): 651-654.

van Dissen, R. and R. S. Yeats (1991). *Hope Fault, Jordan Thrust, and Uplift of the Seaward Kaikoura Range, New-Zealand.* Geology **19**(4): 393-396.

Walcott, R. I. (1978). *Present Tectonics and Late Cenozoic Evolution of New-Zealand.* Geophysical Journal of the Royal Astronomical Society **52**(1): 137-164.

Walcott, R. I. (1979). *Strain-Measurements and Tectonics of New-Zealand.* Tectonophysics **52**(1-4): 479-479.

Walcott, R. I. (1998). *Modes of Oblique Compression: Late Cenozoic Tectonics of the South Island of New Zealand.* Reviews of Geophysics **36**(1): 1-26.

Wessel, P. and W. H. F. Smith (1995). *New Version of the Generic Mapping Tools Released.* EOS Trans. AGU **76**: 329.

Wood, P. R. and G. H. Blick (1986). Some Results of Geodetic Fault Monitoring in South Island New Zealand, In Recent Crustal Movements of the Pacific Region. W. I. Reilly and B. E. Harford (Eds), Bulletin of the Royal Soceity of New Zealand. **24:** 39-45.

Yetton, M. D., A. Wells and N. J. Traylen (1998). The Probablility and Consequences of the Next Alpine Fault Earthquake, New Zealand. Wellington, New Zealand, New Zealand Earthquake Commission. **Earthquake Commission Research Report 95/193:** 161.

Zhang, F. P., D. Dong, Z. Y. Cheng, M. K. Cheng and C. Huang (2002). *Seasonal Vertical Crustal Motions in China Detected by GPS.* Chinese Science Bulletin **47**(21): 1772-1779.

Zhang, J., Y. Bock, H. Johnson, P. Fang, S. Williams, J. Genrich, S. Wdowinski and J. Behr (1997). *Southern California Permanent GPS Geodetic Array - Error Analysis of Daily Position Estimates and Site Velocities.* Journal of Geophysical Research-Solid Earth **102**(B8): 18035-18055.